

PRECISE STRONG LENSING MASS MODELING OF FOUR HUBBLE FRONTIER FIELDS CLUSTERS AND
A SAMPLE OF MAGNIFIED HIGH-REDSHIFT GALAXIESRYOTA KAWAMATA¹, MASAMUNE OGURI^{2,3,4}, MASAFUMI ISHIGAKI^{2,5}, KAZUHIRO SHIMASAKU^{1,3}, AND MASAMI OUCHI^{4,5}*Accepted for publication in ApJ*

ABSTRACT

We conduct precise strong lensing mass modeling of four *Hubble* Frontier Fields (HFF) clusters, Abell 2744, MACS J0416.1–2403, MACS J0717.5+3745, and MACS J1149.6+2223, for which HFF imaging observations are completed. We construct a refined sample of more than 100 multiple images for each cluster by taking advantage of the full depth HFF images, and conduct mass modeling using the GLAFIC software, which assumes simply parametrized mass distributions. Our mass modeling also exploits a magnification constraint from the lensed Type Ia supernova HFF14Tom for Abell 2744 and positional constraints from the multiple images S1–S4 of the lensed supernova SN Refsdal for MACS J1149.6+2223. We find that our best-fitting mass models reproduce the observed image positions with RMS errors of $\sim 0''.4$, which are smaller than RMS errors in previous mass modeling that adopted similar numbers of multiple images. Our model predicts a new image of SN Refsdal with a relative time delay and magnification that are fully consistent with a recent detection of reappearance. We then construct catalogs of $z \sim 6 - 9$ dropout galaxies behind the four clusters and estimate magnification factors for these dropout galaxies with our best-fitting mass models. The dropout sample from the four cluster fields contains ~ 120 galaxies at $z \gtrsim 6$, about 20 of which are predicted to be magnified by a factor of more than 10. Some of the high-redshift galaxies detected in the HFF have lensing-corrected magnitudes of $M_{UV} \sim -15$ to -14 . Our analysis demonstrates that the HFF data indeed offer an ideal opportunity to study faint high-redshift galaxies. All lensing maps produced from our mass modeling will be made available on the STScI website ^a.

Subject headings: galaxies: clusters: individual (Abell 2744, MACS J0416.1–2403, MACS J0717.5+3745, MACS J1149.6+2223) — galaxies: high-redshift — gravitational lensing: strong

1. INTRODUCTION

Studies of faint high-redshift galaxies can be significantly improved by utilizing massive clusters of galaxies as natural telescopes. This is made possible by the so-called gravitational lensing effect, in which the propagation of a light ray is deflected by an intervening matter distribution (Schneider et al. 1992). Although rare, extremely strong lensing events provide an opportunity to study very distant galaxies using their highly magnified images that otherwise cannot even be detected.

The *Hubble* Frontier Fields (HFF; PI: J. Lotz) is an on-going public *Hubble Space Telescope* (*HST*) survey to image six massive clusters. The main purpose of the HFF is to study properties and populations of faint high-redshift galaxies behind the cores of these clusters with help of lensing magnifications. Analyses of early HFF data have already produced useful results on

faint-end luminosity functions of high-redshift galaxies (Coe et al. 2015; Atek et al. 2014, 2015a,b; Ishigaki et al. 2015; Oesch et al. 2015; McLeod et al. 2015), size evolution of galaxies (Kawamata et al. 2015), and deep spectroscopy of faint high-redshift galaxies (Vanzella et al. 2014; Zitrin et al. 2015a).

A key ingredient for the analysis of the HFF data is precise mass modeling of the lensing clusters. This is because we need to convert observed quantities, such as apparent magnitudes and angular sizes of galaxies, to physical quantities such as intrinsic luminosities and physical sizes which require corrections of gravitational lensing effects. The mass distribution of the core of a cluster is usually constrained so that it can reproduce the positions of multiple images behind the cluster. A lot of efforts had been made for mass modeling before the HFF observations started, using pre-HFF data, in order to allow prompt analyses of the HFF data by the community (e.g., Richard et al. 2014; Johnson et al. 2014; Zitrin et al. 2015b).

The accuracy of mass modeling relies on the number of multiply imaged background galaxies. Much deeper *HST* images obtained by the HFF in fact allow one to identify many more multiply imaged galaxies and therefore improve strong lensing mass modeling (e.g., Jauzac et al. 2014, 2015a; Lam et al. 2014; Diego et al. 2015a,b; Limousin et al. 2015). In addition, spectroscopy of these multiple images is crucial for robust identification of multiple images as well as constraining the mass distribution, particularly the radial density pro-

Email: kawamata@astron.s.u-tokyo.ac.jp

¹ Department of Astronomy, Graduate School of Science, The University of Tokyo, 7-3-1 Hongo, Bunkyo-ku, Tokyo 113-0033, Japan

² Department of Physics, Graduate School of Science, The University of Tokyo, 7-3-1 Hongo, Bunkyo-ku, Tokyo 113-0033, Japan

³ Research Center for the Early Universe, The University of Tokyo, 7-3-1 Hongo, Bunkyo-ku, Tokyo 113-0033, Japan

⁴ Kavli Institute for the Physics and Mathematics of the Universe (Kavli IPMU, WPI), The University of Tokyo, 5-1-5 Kashiwanoha, Kashiwa, Chiba 277-8583, Japan

⁵ Institute for Cosmic Ray Research, The University of Tokyo, 5-1-5 Kashiwanoha, Kashiwa, Chiba 277-8582, Japan

^a <https://archive.stsci.edu/prepds/frontier/lensmodels/>

file. Significant efforts are being made to collect spectroscopic redshifts of galaxies detected in the HFF (e.g., Schmidt et al. 2014; Grillo et al. 2015a; Karman et al. 2015; Wang et al. 2015; Treu et al. 2015b; Sebesta et al. 2015).

In this paper, we present our mass modeling results of the first four HFF clusters, Abell 2744 (Abell 1958), MACS J0416.1–2403 (Mann & Ebeling 2012), MACS J0717.5+3745 (Ebeling et al. 2007), and MACS J1149.6+2223 (Ebeling et al. 2007), using the full-depth HFF data as well as the latest follow-up data. For each cluster we use more than 100 multiple images to constrain the mass distribution assuming a simply parametrized mass model. We then construct $z \sim 6 - 9$ dropout galaxy catalogs in these clusters. Our mass modeling results are used to derive magnification factors for these high-redshift galaxies. We also discuss whether these high-redshift galaxies are multiply imaged or not.

The structure of our paper is as follows. In Section 2, we describe the *HST* data used in the paper, as well as the construction of photometric catalogs. Our mass modeling procedure is described in detail in Section 3, and the results of the mass modeling are given in Section 4. We construct $z \sim 6 - 9$ dropout galaxy catalogs in Section 5. Finally, we summarize our results in Section 6. Throughout this paper, we adopt a flat cosmological model with the matter density $\Omega_M = 0.3$, the cosmological constant $\Omega_\Lambda = 0.7$, and the Hubble constant $H_0 = 70 \text{ km s}^{-1} \text{ Mpc}^{-1}$. Magnitudes are given in the AB system (Oke & Gunn 1983) and coordinates are given in J2000.

2. *HST* DATA

2.1. *HST* Images

We use the public HFF data⁷ for our analysis. The HFF targets six massive clusters, Abell 2744 ($z = 0.308$), MACS J0416.1–2403 ($z = 0.397$), MACS J0717.5+3745 ($z = 0.545$), MACS J1149.6+2223 ($z = 0.541$), Abell S1063 ($z = 0.348$), and Abell 370 ($z = 0.375$), which have been chosen according to their lensing strength and also their accessibility from major ground-based telescopes. The cluster core and parallel field region of each cluster are observed deeply with the IR channel of Wide Field Camera 3 (WFC3/IR) and the Advanced Camera for Surveys (ACS). As of October 2015, *HST* observations for the first four clusters, Abell 2744, MACS J0416.1–2403, MACS J0717.5+3745, and MACS J1149.6+2223, are completed. Observations of the remaining two clusters will be completed by mid 2016.

In this study, we use the Version 1.0 data products of drizzled images with a pixel scale of $0''.03 \text{ pixel}^{-1}$ provided by Space Telescope Science Institute (STScI). The images for each cluster consist of F435W (B_{435}), F606W (V_{606}), and F814W (i_{814}) images from ACS, and F105W (Y_{105}), F125W (J_{125}), F140W (JH_{140}), and F160W (H_{160}) images from WFC3/IR. While we use standard correction mosaics for the ACS images, we choose mosaics corrected for time-variable background sky emission for the WFC3/IR images when available. In order to take account of the inhomogeneity of the limiting magnitude due to, e.g., intracluster light, we divide

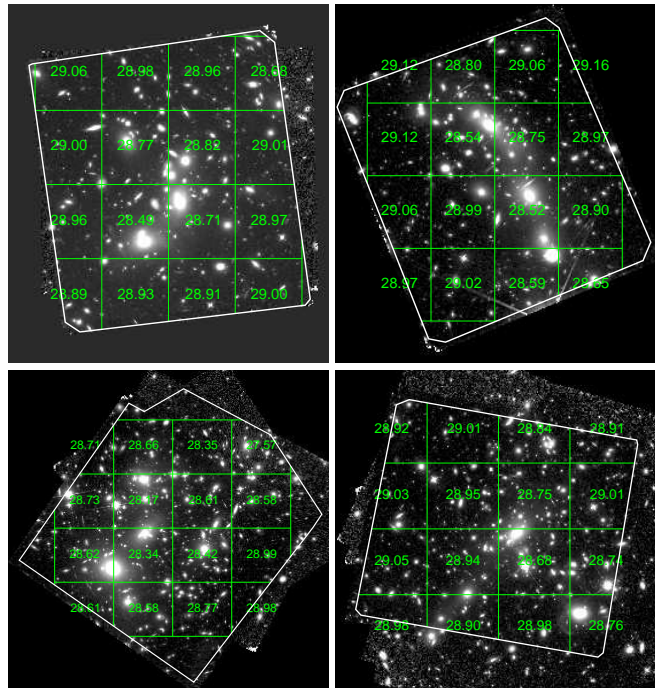


Figure 1. Measured 5σ limiting magnitudes in 4×4 grid cells. H_{160} limiting magnitudes are shown on the *HST* H_{160} band image for Abell 2744 (upper left), MACS J0416.1–2403 (upper right), MACS J0717.5+3745 (lower left), and MACS J1149.6+2223 (lower right). Each number shows the limiting magnitude in each cell. We use only the regions within the white lines to search for high-redshift galaxies.

the WFC3/IR field of view of each cluster into 4×4 grid cells and measure limiting magnitudes in individual cells, as shown in Figure 1. The 5σ limiting magnitudes on a $0''.35$ diameter aperture of these images are ~ 29 mag.

Three out of the four clusters have also been observed with *HST* in the CLASH project (see Postman et al. 2012, for more details). Although the CLASH imaging uses many additional bands (F225W, F275W, F336W, F390W, F475W, F625W, F775W, F850LP, and F110W), we do not use these images because they are considerably shallower than the HFF images.

2.2. Photometric Catalogs

We construct two different photometric catalogs specified for the following two purposes, (1) selection of cluster member galaxies and (2) detection of faint high-redshift galaxies, using the method similar to the one used in Ishigaki et al. (2015). Here we briefly describe the method to construct the photometric catalogs.

Member galaxies are selected utilizing both the red sequence and photometric redshift techniques. For accurate estimates of galaxy colors, we convolve *HST* images with a Gaussian kernel in order to match the point-spread function (PSF) sizes of all images of interest to the largest one. Then, we run SEXTRACTOR (Bertin & Arnouts 1996) in dual-image mode using the i_{814} image as the detection image setting the parameters DEBLEND_MINCONT = 0.00005, DEBLEND_NTHRESH = 50, DETECT_MINAREA = 5, and DETECT_THRESH = 2.5. We estimate photometric redshifts of the galaxies in this catalog using BPZ (Benítez 2000). We use the $B_{435}-V_{606}$ color-magnitude diagram to identify the red sequence, and extract cluster members with V_{606} -band magnitudes

⁷ <http://www.stsci.edu/hst/campaigns/frontier-fields/>

brighter than $\sim 24 - 25$ mag (see Ishigaki et al. 2015, for more details). We then select galaxies in the vicinity of the red sequence whose photometric redshifts coincide with the cluster redshift as cluster members. After applying these criteria, we refine the member galaxy catalog by adding and removing some galaxies based on their colors, morphologies, and spectroscopic redshifts (Owers et al. 2011; Ebeling et al. 2014).

In the construction of a photometric catalog of high-redshift galaxies, we co-add three bands (J_{125} , JH_{140} , and H_{160}) for the i - and Y -dropout selection and two bands (JH_{140} and H_{160}) for the YJ -dropout selection using SWARP (Bertin et al. 2002). Weight images of these co-added images are also produced from public weight images. Before running SExtractor to build photometric catalogs, we again match PSF sizes for reliable color measurements. For the i -dropout selection, images for all the bands are PSF-matched except for B_{435} and V_{606} , and for the other selections all except for B_{435} , V_{606} , and i_{814} are PSF-matched. Then, we run SExtractor in dual-image mode using the co-added images as the detection image with the parameters of DEBLEND_MINCONT = 0.0005, DEBLEND_NTHRESH = 16, DETECT_MINAREA = 4, and DETECT_THRESH = 3.0. For measuring colors of galaxies, we use aperture magnitudes (MAG_APER) m_{AP} with a aperture diameter of $0''.35$ for the convolved images and $0''.20$ (B_{435}), $0''.19$ (V_{606}), and $0''.19$ (i_{814}) for the non-convolved images. Total magnitudes of galaxies are also derived from MAG_APER magnitudes with the aperture correction derived in Ishigaki et al. (2015). Specifically, the aperture correction factor c_{AP} is $c_{AP} = 0.82$, which is defined such that the total magnitude m_{tot} is given by $m_{tot} = m_{AP} - c_{AP}$.

We also derive photometric redshifts for the high-redshift galaxies detected in the second photometric catalog using BPZ. For reliable color measurements, we PSF-match all the band images. The photometric redshifts are used to both identify multiple images (see Section 3) and select high-redshift galaxies (see Section 5).

3. MASS MODELING PROCEDURE

Here we describe the method to model the mass distributions of the four HFF clusters in detail. We adopt the so-called “parametric lens modeling” approach, in which a simply parametrized mass model consisting of several mass components is assumed and the model parameters are optimized to reproduce observed multiple image properties. Throughout the paper mass modeling and analysis are performed using the public software GLAFIC (Oguri 2010), which has extensively been used for strong lensing mass modeling of clusters (e.g., Oguri et al. 2012, 2013; Köhlinger & Schmidt 2014; Ishigaki et al. 2015; Newman et al. 2015).

3.1. Mass Components

In this paper we adopt the following mass components. Details of each mass component are described in Oguri (2010). We give a brief summary below.

A cluster-scale dark halo is modeled by an elliptical extension of the NFW (Navarro et al. 1997) density profile. We introduce an elliptical symmetry in the projected mass density, and compute its lensing properties by numerical integrals (Schramm 1990). The model parameters include virial mass M , positions, ellipticity

$e \equiv 1 - a/b$ (a and b being minor and major axis lengths, respectively) and its position angle θ_e , and concentration parameter c .

Member galaxies are modeled by pseudo-Jaffe ellipsoids (Keeton 2001). To reduce the number of parameters, in most cases we introduce scaling relations of model parameters with luminosity L , such that velocity dispersion is given by $\sigma/\sigma_* \propto L^{1/4}$ and truncation radius $r_{trun}/r_{trun,*} \propto L^\eta$. The ellipticity and position angle of each galaxy are fixed to the values measured by SExtractor. All the input quantities for the member galaxies are measured in the i_{814} band. Luminosities are computed from total magnitudes (MAG_AUTO) given by SExtractor. The model parameters are the normalization of velocity dispersion σ_* , truncation radius $r_{trun,*}$, and dimensionless parameter η . We call this model of a set of member galaxies GALs.

Member galaxies that are located adjacent to multiple images can have significant contributions to the image properties of the multiple images including their locations. For some of these member galaxies we do not apply the scaling relations mentioned above but instead model them independently by pseudo-Jaffe ellipsoid components, to which we refer as PJE. The model parameters are velocity dispersion σ , ellipticity e and its position angle θ_e , and truncation radius r_{trun} .

It has been shown that adding an external perturbation on the lens potential and an internal perturbation describing a possible asymmetry of the cluster mass distribution sometimes improves the mass model significantly (e.g., Oguri 2010; Oguri et al. 2013). Both perturbations are described by a multipole Taylor expansion at the position of the BCG of the form $\phi = (C/m)r^n \cos m(\theta - \theta_*)$, where r is the distance from the BCG, θ is angular coordinate, θ_* is position angle, and C is expansion coefficient. In the case of the external perturbation, the zeroth ($n = 0$, $m = 0$) and the first ($n = 1$, $m = 1$) orders of the Taylor expansion are unobservable. We call the second order term of the external perturbation ($n = 2$, $m = 2$), which is equivalent to the so-called external shear, PERT. We also include higher multipole terms ($m \geq 3$) to approximately model higher-order terms of the external perturbation as well as a possible asymmetry of the cluster mass distribution, which we refer to as MPOLE. Note that a term inducing constant convergence κ ($n = 2$, $m = 0$) is not included in our mass modeling.

The amplitudes of the perturbations are defined for a given fiducial source redshift $z_{s,fd}$, and are scaled with the source redshift assuming that the perturbation originates from the structure at the cluster redshift. The model parameters for PERT are external shear γ and its position angle θ_γ , and those for MPOLE are expansion coefficient ϵ , position angle θ_e , m , and n . The values of γ and ϵ are assumed to be constant over the entire field.

3.2. Modeling Strategy

We adopt the following unified strategy for conducting our mass modeling. We place several NFW components on the positions of bright cluster member galaxies. When an NFW component has a sufficient number of multiple images around it to constrain the model parameters well, all the NFW model parameters are treated as free parameters. On the other hand, for NFW components

located at the edge or outside the strong lensing regions, we fix some model parameters such as positions, ellipticities, and position angles, to observed values. For NFW components lacking strong observational constraints, it is also difficult to reliably constrain the concentration parameter c . In this case we simply assume $c = 10$.

We start with a small number of NFW components, and increase the number of components until we find the least reduced χ^2 . We stop adding an NFW component when it begins to increase the reduced χ^2 , which is caused because a decrease in the degree of freedom surpasses an improvement in the raw χ^2 . Perturbations (PERT and MPOLE) are also added as long as they improve the mass model significantly. In parallel with building the mass model, we iteratively refine multiple images used as constraints, by validating known multiple image candidates and searching for new multiple image candidates. New multiple image candidates are identified based on consistency with the mass model and on colors, morphologies, and photometric redshifts. Our selection of multiple images is conservative in the sense that we remove any unreliable or suspicious candidates. A final set of multiple images for each cluster is given in Section 3.4.

About one fifth of the multiple images have spectroscopic redshifts. The source redshifts are fixed to the spectroscopic redshifts when available. The redshifts of the other multiple images are treated as model parameters and are optimized together with source positions. Some multiple images have a precise photometric redshift estimate. For them, we include this information in the optimization by adding a Gaussian prior centered at the estimated redshift and a conservative standard deviation of $\sigma_z = 0.5$ (see also below). We choose this conservative value in order not to avoid any bias in the best-fitting mass model originating from potential biases in our photometric redshift estimates.

3.3. Optimizations and Error Estimates

All the model parameters are simultaneously optimized to reproduce the positions and photometric redshifts of the multiple images. Specifically, the optimization is performed to minimize χ^2

$$\chi^2 = \chi_{\text{pos}}^2 + \chi_z^2, \quad (1)$$

$$\chi_{\text{pos}}^2 = \sum_i \frac{|\mathbf{x}_{i,\text{obs}} - \mathbf{x}_i|^2}{\sigma_{x_i}^2}, \quad (2)$$

$$\chi_z^2 = \sum_j \frac{(z_{j,\text{obs}} - z_j)^2}{\sigma_z^2}, \quad (3)$$

where \mathbf{x}_i is the position of the i -th image and z_j is the source redshift of the j -th system. The positional uncertainties $\sigma_{x,i}$ can be different for different images and are given in Section 3.4. For Abell 2744, we include an additional term $\chi_\mu^2 = (\mu_{\text{obs}} - \mu)^2 / \sigma_\mu^2$ from the observation of a Type Ia supernova behind this cluster (see Section 3.4 for more details).

Formally we need to solve a non-linear lens equation to estimate the position χ^2 (Equation 2), which is time-consuming. We adopt the so-called source plane minimization which evaluates Equation (2) in the source plane. Once a distance in the source plane is converted to a corresponding distance in the image plane using the full

magnification tensor, this provides a very good approximation for the image plane position χ^2 (see Appendix 2 of Oguri 2010).

We derive the best-fitting mass model for each cluster that minimizes the total χ^2 (Equation 1) by a standard downhill simplex method. In addition, we run Markov Chain Monte Carlo (MCMC) to estimate errors in the mass models. When deriving the best-fitting mass model and running MCMC, the parameter ranges of ellipticity, concentration parameter, and index η for GALs are restricted to $[0, 0.8]$, $[1, 40]$, and $[0.2, 1.5]$, respectively.

3.4. Input Data for Each Cluster

3.4.1. Abell 2744

Multiple images for this cluster have been identified in Merten et al. (2011), Atek et al. (2014), Richard et al. (2014), Zitrin et al. (2014), Lam et al. (2014), Ishigaki et al. (2015), and Jauzac et al. (2015a). Spectroscopic redshifts of multiple images have been presented in Richard et al. (2014), Johnson et al. (2014), and Wang et al. (2015). Lam et al. (2014) and Wang et al. (2015) regarded systems 55 and 56 as a part of systems 1 and 2, respectively, and assigned their redshifts accordingly. To avoid introducing biases, we do not fix the redshifts but treat them as model parameters. While Wang et al. (2015) reported the redshift of system 56 to be $z = 1.2$ with a rating of probable, Johnson et al. (2014) estimated it to be $z = 2.2$ and Lam et al. (2014) adopted this value in their mass modeling. In our mass modeling, we do not assume any spectroscopic redshift on this system and find a model-predicted redshift of $z = 1.87_{-0.07}^{+0.07}$, which is closer to that of Johnson et al. (2014). Due to a controversy over the position of the counter image of system 3 (see e.g. Lam et al. 2014; Jauzac et al. 2015a, for more details), we do not use its position as a constraint in our mass modeling. For system 5, we find one new counter image. Although Wang et al. (2015) recently reported the redshift of system 22 to be $z = 4.84$, we do not adopt this value because it is not very secure. We identify a new set of multiple images (system 62) in the northwest part of this cluster. As noted above, we conservatively exclude some multiple images in the literature. As a result, we have 37 multiple image systems from the literature and one new system for our mass modeling. The total number of multiple images is 111. The positional uncertainty of $\sigma_x = 0''.4$ is assumed for all of them.

In addition we include a magnification constraint at the position of the type Ia supernova HFF14Tom at $z = 1.3457$ (Rodney et al. 2015a). The magnification of the HFF14Tom is estimated by a careful cosmology-independent analysis to be $\mu = 2.03 \pm 0.29$. We use this constraint by adding a term to the total χ^2 (Equation 1).

3.4.2. MACS J0416.1–2403

Multiple images for this cluster have been identified in Zitrin et al. (2013), Jauzac et al. (2014), and Diego et al. (2015a). Spectroscopic redshifts of multiple images have been presented in Christensen et al. (2012) and Grillo et al. (2015a). We also use new spectroscopic redshifts from GLASS (Hoag et al. in prep.; see also Schmidt et al. 2014 and Treu et al. 2015b) and Rodney et al. (in prep.). While Jauzac et al. (2014) estimated

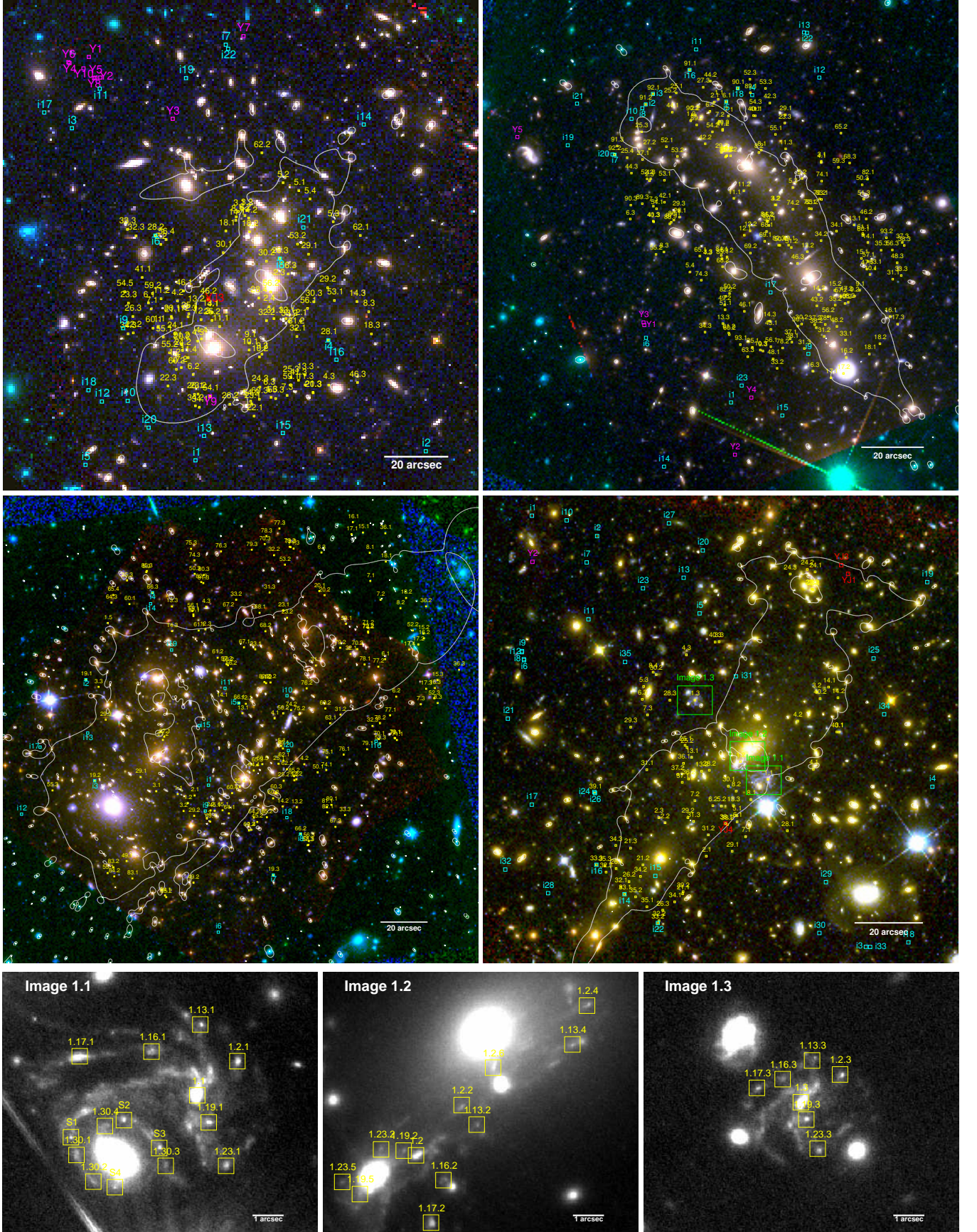


Figure 2. Multiple image systems used for mass modeling, dropout galaxies, and critical curves of the best-fitting models for Abell 2744 (upper left), MACS J0416.1-2403 (upper right), MACS J0717.5+3745 (middle left), and MACS J1149.6+2223 (middle right). Underlying color-composite images are created from the *HST* $B_{435}+V_{606}$, $i_{814}+Y_{105}$, $J_{125}+JH_{140}+H_{160}$ band images. Small yellow squares show the positions of multiple images (see Appendix A for the coordinates). High-redshift dropout galaxies are marked with large squares (see Section 5 for details). Critical curves for a source redshift of $z = 8$ are shown with the solid lines. Bottom panels show zoomed in *HST* i_{814} -band images of the system 1 in the MACS J1149.6+2223 field. Small yellow squares represent the positions of multiply imaged knots that are used as constraints in mass modeling.

Table 1
Summary of mass modeling

Cluster	# of multiple image systems (with spec- z)	# of multiple images	χ^2/dof	Image plane RMS (")
Abell 2744	38 (5)	111	98.2/100	0.37
MACS J0416.1–2403	68 (16)	182	155.8/168	0.44
MACS J0717.5+3745	60 (8)	173	144.5/144	0.52
MACS J1149.6+2223	36 (16)	108	100.1/103	0.31

Table 2
Mass Model Parameters for Abell 2744

Component	Model	Mass ($10^{14} h^{-1} M_{\odot}$)	e	θ_e (deg)	c	Δx^a (arcsec)	Δy^a (arcsec)
Cluster halo 1	NFW	$4.46^{+2.35}_{-1.36}$	$0.45^{+0.04}_{-0.04}$	$152.23^{+2.26}_{-2.56}$	$3.39^{+0.66}_{-0.53}$	$-0.28^{+0.37}_{-0.40}$	$0.20^{+0.42}_{-0.43}$
Cluster halo 2	NFW	$1.57^{+0.23}_{-0.24}$	$0.42^{+0.03}_{-0.03}$	$132.78^{+1.67}_{-0.90}$	$8.46^{+0.54}_{-0.49}$	$-18.51^{+0.26}_{-0.26}$	$-17.91^{+0.22}_{-0.23}$
Cluster halo 3	NFW	$0.36^{+0.07}_{-0.06}$	$0.79^{+0.01}_{-0.02}$	$101.97^{+2.87}_{-2.81}$	[10.00]	[−26.97]	[30.91]
		σ_*^b (km s $^{-1}$)	$r_{\text{trun},*}$ (")	η			
Member galaxies	GALS	$208.73^{+7.61}_{-7.77}$	$82.71^{+29.72}_{-28.75}$	$1.25^{+0.16}_{-0.20}$			
		$z_{s,\text{fid}}$	γ	θ_γ (deg)			
External perturbation	PERT	[2.00]	$0.05^{+0.02}_{-0.02}$	$138.75^{+4.24}_{-7.63}$			
		$z_{s,\text{fid}}$	ϵ	θ_ϵ (deg)	m	n	
Multipole perturbation	MPOLE	[2.00]	$0.01^{+0.00}_{-0.00}$	$85.41^{+3.31}_{-2.88}$	[3.00]	[2.00]	

^a Coordinates are relative to the brightest cluster galaxy position in the Abell 2744 field (R.A. = 3.58611, Decl. = −30.40024).

^b The normalization luminosity L^* corresponds to $i_{814} = 18.33$.

* Numbers in square brackets are fixed during the model optimization.

Table 3
Mass Model Parameters for MACS J0416.1–2403

Component	Model	Mass ($10^{14} h^{-1} M_{\odot}$)	e	θ_e (deg)	c	Δx^a (arcsec)	Δy^a (arcsec)
Cluster halo 1	NFW	$3.22^{+1.06}_{-0.76}$	$0.64^{+0.02}_{-0.02}$	$56.59^{+1.69}_{-1.64}$	$4.20^{+0.42}_{-0.37}$	$-2.09^{+0.65}_{-0.51}$	$1.39^{+0.42}_{-0.44}$
Cluster halo 2	NFW	$1.90^{+0.97}_{-0.66}$	$0.64^{+0.03}_{-0.03}$	$42.07^{+1.70}_{-1.51}$	$5.31^{+1.26}_{-0.94}$	$22.18^{+0.76}_{-0.67}$	$-35.65^{+0.51}_{-0.57}$
Cluster halo 3	NFW	$0.51^{+0.21}_{-0.15}$	$0.61^{+0.03}_{-0.08}$	$40.41^{+3.86}_{-4.17}$	$5.95^{+1.30}_{-1.02}$	$25.68^{+0.97}_{-1.38}$	$-55.26^{+1.62}_{-1.02}$
		σ_*^b (km s $^{-1}$)	$r_{\text{trun},*}$ (")	η			
Member galaxies	GALS	$261.59^{+21.36}_{-17.44}$	$24.04^{+10.02}_{-6.09}$	$1.31^{+0.12}_{-0.15}$			
		σ (km s $^{-1}$)	e	θ_e (deg)	r_{trun} (")	Δx^a (arcsec)	Δy^a (arcsec)
Member galaxy	PJE	$125.29^{+50.22}_{-19.36}$	[0.27]	[166.70]	$0.70^{+1.38}_{-0.47}$	[−14.56]	[15.28]
		$z_{s,\text{fid}}$	γ	θ_γ (deg)			
External perturbation	PERT	[2.00]	$0.06^{+0.01}_{-0.01}$	$35.50^{+3.83}_{-4.40}$			
		$z_{s,\text{fid}}$	ϵ	θ_ϵ (deg)	m	n	
Multipole perturbation	MPOLE	[2.00]	$0.01^{+0.00}_{-0.00}$	$65.07^{+5.96}_{-5.10}$	[3.00]	[2.00]	

^a Coordinates are relative to the brightest cluster galaxy position in the MACS J0416.1–2403 field (R.A. = 64.0380981, Decl. = −24.0674834).

^b The normalization luminosity L^* corresponds to $i_{814} = 18.73$.

* Numbers in square brackets are fixed during the model optimization.

Table 4
Mass Model Parameters for MACS J0717.5+3745

Component	Model	Mass ($10^{14} h^{-1} M_{\odot}$)	e	θ_e (deg)	c	Δx^a (arcsec)	Δy^a (arcsec)
Cluster halo 1	NFW	$4.78^{+1.02}_{-0.59}$	$0.63^{+0.03}_{-0.03}$	$135.70^{+1.43}_{-1.09}$	$3.97^{+0.36}_{-0.53}$	$8.09^{+1.05}_{-0.62}$	$3.44^{+1.11}_{-0.79}$
Cluster halo 2	NFW	$2.02^{+0.20}_{-0.39}$	$0.73^{+0.02}_{-0.02}$	$135.60^{+0.95}_{-1.46}$	$3.96^{+0.23}_{-0.31}$	$35.81^{+1.13}_{-0.79}$	$-9.95^{+0.97}_{-0.89}$
Cluster halo 3	NFW	$2.23^{+0.25}_{-0.29}$	$0.56^{+0.02}_{-0.02}$	$142.09^{+1.02}_{-1.32}$	$6.98^{+1.49}_{-1.49}$	$-2.12^{+0.52}_{-0.48}$	$30.13^{+1.11}_{-0.79}$
Cluster halo 4	NFW	$3.18^{+0.48}_{-0.28}$	$0.31^{+0.04}_{-0.04}$	$152.04^{+2.86}_{-1.97}$	$3.85^{+0.31}_{-0.39}$	$67.18^{+0.58}_{-0.61}$	$49.61^{+0.61}_{-0.57}$
Cluster halo 5	NFW	$1.51^{+0.08}_{-0.13}$	[0.32]	[174.30]	[10.00]	[129.13]	[77.20]
Cluster halo 6	NFW	$0.56^{+0.13}_{-0.13}$	$0.19^{+0.23}_{-0.12}$	$105.68^{+1.57}_{-2.84}$	$2.39^{+0.53}_{-0.55}$	[-19.33]	[-21.66]
Cluster halo 7	NFW	$1.20^{+0.16}_{-0.19}$	$0.55^{+0.04}_{-0.04}$	$129.81^{+1.33}_{-1.61}$	$3.56^{+0.49}_{-0.53}$	[108.64]	[45.46]
Cluster halo 8	NFW	$0.14^{+0.02}_{-0.03}$	$0.78^{+0.02}_{-0.02}$	$146.46^{+4.24}_{-1.51}$	$2.69^{+0.56}_{-0.68}$	[-10.32]	[-42.04]
Cluster halo 9	NFW	$0.06^{+0.05}_{-0.02}$	$0.76^{+0.03}_{-0.04}$	$133.99^{+4.15}_{-4.48}$	$12.40^{+5.93}_{-4.83}$	$29.63^{+2.05}_{-2.53}$	$-32.35^{+1.20}_{-0.99}$
		σ_*^b (km s^{-1})	$r_{\text{trun},*}$ ($''$)	η			
Member galaxies	GALS	$518.64^{+35.12}_{-43.24}$	$7.06^{+2.25}_{-2.08}$	$0.43^{+0.07}_{-0.09}$			
		$z_{s,\text{fid}}$	γ	θ_γ (deg)			
External perturbation	PERT	[2.00]	$0.12^{+0.00}_{-0.01}$	$51.13^{+1.49}_{-0.90}$	m	n	
		$z_{s,\text{fid}}$	ϵ	θ_ϵ (deg)			
Multipole perturbation 1	MPOLE	[2.00]	$0.02^{+0.00}_{-0.00}$	$42.99^{+2.36}_{-7.54}$	[3.00]	[2.00]	
Multipole perturbation 2	MPOLE	[2.00]	$0.01^{+0.00}_{-0.00}$	$8.54^{+2.99}_{-1.74}$	[4.00]	[2.00]	
Multipole perturbation 3	MPOLE	[2.00]	$0.01^{+0.00}_{-0.00}$	$20.00^{+1.44}_{-1.75}$	[5.00]	[2.00]	

^a Coordinates are relative to the brightest cluster galaxy position in the MACS J0717.5+3745 field (R.A. = 109.3982391, Decl. = +37.7457307).

^b The normalization luminosity L^* corresponds to $i_{814} = 17.16$.

* Numbers in square brackets are fixed during the model optimization.

Table 5
Mass Model Parameters for MACS J1149.6+2223

Component	Model	Mass ($10^{14} h^{-1} M_{\odot}$)	e	θ_e (deg)	c	Δx^a (arcsec)	Δy^a (arcsec)
Cluster halo 1	NFW	$8.26^{+1.52}_{-1.83}$	$0.49^{+0.02}_{-0.02}$	$126.37^{+1.31}_{-1.28}$	$3.82^{+0.34}_{-0.25}$	$-0.21^{+0.15}_{-0.16}$	$-0.12^{+0.10}_{-0.10}$
Cluster halo 2	NFW	$1.61^{+0.59}_{-0.46}$	$0.67^{+0.09}_{-0.14}$	$76.36^{+7.39}_{-6.88}$	$6.66^{+2.75}_{-2.16}$	[16.38]	[47.36]
Cluster halo 3	NFW	$0.64^{+0.75}_{-0.34}$	$0.70^{+0.05}_{-0.06}$	$158.13^{+3.19}_{-4.23}$	$2.57^{+1.50}_{-0.85}$	$-22.93^{+1.04}_{-0.68}$	$-32.21^{+1.31}_{-1.26}$
Cluster halo 4	NFW	$0.16^{+0.04}_{-0.03}$	$0.68^{+0.08}_{-0.10}$	$150.23^{+2.05}_{-2.71}$	[10.00]	[-44.77]	[-54.86]
		σ_*^b (km s^{-1})	$r_{\text{trun},*}$ ($''$)	η			
Member galaxies	GALS	$233.07^{+21.42}_{-16.80}$	$2.88^{+1.07}_{-0.65}$	$0.26^{+0.08}_{-0.04}$	r_{trun}	Δx^a	Δy^a
		σ (km s^{-1})	e	θ_e (deg)	r_{trun} ($''$)	(arcsec)	(arcsec)
Member galaxy ^c	PJE	$232.08^{+25.96}_{-17.38}$	[0.30]	[47.50]	$1.26^{+0.54}_{-0.38}$	[3.22]	[-11.11]
		$z_{s,\text{fid}}$	γ	θ_γ (deg)			
External perturbation	PERT	[2.00]	$0.04^{+0.02}_{-0.01}$	$82.76^{+9.28}_{-7.17}$	m	n	
		$z_{s,\text{fid}}$	ϵ	θ_ϵ (deg)			
Multipole perturbation	MPOLE	[2.00]	$0.02^{+0.00}_{-0.00}$	$165.09^{+4.04}_{-3.37}$	[3.00]	[2.00]	

^a Coordinates are relative to the brightest cluster galaxy position in the MACS J1149.6+2223 field (R.A. = 177.3987491, Decl. = +22.3985308).

^b The normalization luminosity L^* corresponds to $i_{814} = 18.80$.

^c This component corresponds to the member galaxy that produces four multiple images S1–S4 of SN Refsdal.

* Numbers in square brackets are fixed during the model optimization.

the redshift of system 14 to be $z = 2.0531$, Grillo et al. (2015a) reported that its correct redshift is $z = 1.637$. We adopt the latter as it reproduces its image positions well. We correct the positions of five counter images, 29.2, 37.3, 40.3, 41.3, and 55.2, and add nine new systems, 74, 78, 82, 83, 89, 90, 91, 92, and 93, and identify four new counter images, 6.3, 8.3, 34.3, and 50.3. As a result, we have 59 multiple image systems from the literature and nine new systems for our mass modeling. The total number of multiple images is 182. The positional uncertainty of $\sigma_x = 0''.4$ is assumed for all of them.

3.4.3. MACS J0717.5+3745

Multiple images for this cluster have been identified in Zitrin et al. (2009), Limousin et al. (2012), Vanzella et al. (2014), Richard et al. (2014), and Diego et al. (2015b). Spectroscopic redshifts of multiple images have been presented in Limousin et al. (2012), Schmidt et al. (2014), Vanzella et al. (2014), and Treu et al. (2015b). The redshift of system 5 was newly confirmed and those of systems 12 and 13 were updated by GLASS (Schmidt et al. 2014; Treu et al. 2015b). While we use the updated redshift of system 12, we do not use that of system 5 as it is significantly different from our model prediction and that of system 13 as it is less precise than that estimated in Limousin et al. (2012). We assign image 25.4 to system 25, which was regarded as a part of system 5 in Diego et al. (2015b). We add six new counter images, 25.4, 55.3, 64.3, 64.4, 65.3, and 65.4, and 20 new systems, 66 – 85. As a result, we have 40 multiple image systems from the literature and 20 new systems for our mass modeling. The total number of multiple images is 173. As a foreground galaxy located at (R.A. = 109.405027, Decl. = +37.739714) makes a significant contribution to the lensing effect, we independently model this galaxy by an NFW, but at the cluster redshift (Cluster halo 6) because GLAFIC does not support multiple lens planes. We assume a positional uncertainty of $\sigma_x = 0''.6$, which is larger than those for the other HFF clusters, for all multiple images. The larger positional uncertainty and the large number of mass components are due to the fact that the mass distribution of this cluster appears to be considerably more complicated than the other clusters, presumably due to ongoing multiple mergers (see, e.g., Limousin et al. 2012).

3.4.4. MACS J1149.6+2223

Multiple images for this cluster have been identified in Zitrin & Broadhurst (2009), Smith et al. (2009), Zheng et al. (2012), Rau et al. (2014), Richard et al. (2014), Jauzac et al. (2015b), and Treu et al. (2015a). Spectroscopic redshifts of multiple images have been presented in Smith et al. (2009), Jauzac et al. (2015b), Grillo et al. (2015b), and Brammer et al. (in prep.). While Smith et al. (2009) estimated the redshift of system 3 to be $z = 2.497$, a recent study using GMOS and MUSE data (Jauzac et al. 2015b; Grillo et al. 2015b) revised its redshift to be $z = 3.129$, which we adopt in our analysis. The new spectroscopic redshifts of system 13 by GLASS (Brammer et al. in prep.) and systems 4, 14, and 29 by MUSE (Grillo et al. 2015b) are used in our mass modeling (see also Treu et al. 2015a). As a result, we have 10 multiple image systems from the literature and 18 new systems, 21 – 40, for our mass modeling. We

also include additional positional constraints from multiple images of seven knots in a lensed face-on spiral galaxy at $z = 1.488$ as well as four supernova images of SN Refsdal in the lensed spiral galaxy (Kelly et al. 2015b). The total number of multiple images is 108 from 36 systems.

In order to accurately predict the reappearance of SN Refsdal image (Oguri 2015; Sharon & Johnson 2015; Diego et al. 2015c; Jauzac et al. 2015b; Grillo et al. 2015b) and its magnification, we follow Oguri (2015) to adopt different positional errors for different multiple images. Specifically, we assume the standard positional error of $\sigma_x = 0''.4$ for most multiple images, but use a smaller error of $\sigma_x = 0''.2$ for the core and knots of the lensed spiral galaxy, and an even smaller error of $\sigma_x = 0''.05$ for the four SN images. A member galaxy located at R.A. = 177.397784, Decl. = +22.395446 clearly has a significant impact on the prediction of the quadruple images S1–S4 of SN Refsdal. Thus we model this galaxy separately by a PJE.

4. MASS MODELING RESULTS

4.1. The best-fitting mass models

The numbers of input multiple images and mass modeling results of the four HFF clusters are summarized in Table 1, and the critical curves of the best-fitting models are shown in Figure 2. Figure 3 shows magnification maps for sources at $z = 9$ and the positions of the NFW and PJE components. We provide lists of all multiple images used as constraints in Appendix A. Model parameters and errors from the MCMC for individual clusters are shown in Tables 2–5. Parameters in square brackets are fixed during the model optimization. Maps of magnification factor, lens potential, kappa, and shear from our mass modeling will be made available on the STScI website⁸.

Table 1 indicates that all of our best-fitting models have reduced chi-square values, χ^2/dof , close to unity. In fact this is expected, because we have chosen the positional errors of multiple images to reproduce $\chi^2/\text{dof} \sim 1$ (see Section 3.4 for the specific values). In cluster strong lensing modeling, the positional errors usually originate from the complexity of the lens potential due to, e.g., substructures that is not included by a simply parametrized model, rather than from measurement uncertainties in multiple image positions. A proper choice of positional uncertainties is important for the MCMC to estimate model uncertainties.

It is found that our best-fitting mass models reproduce the positions of multiple images with RMS errors of $\sim 0''.4$ (see Table 1), which is a significant improvement over previous strong lens modeling (e.g., Broadhurst et al. 2005) and is comparable or even better than other mass models constructed for HFF. For instance, this number should be compared with RMS errors of $0''.68$ for MACS J0416.1–2403 (Jauzac et al. 2014) and $0''.79$ for Abell 2744 (Jauzac et al. 2015a) by the CATS team, both of which used more than 100 multiple images as constraints. Grillo et al. (2015a) modeled MACS J0416.1–2403 with RMS errors of $0''.36$, but only 30 multiple images were used as constraints. Our mass modeling satisfies both a large number of multiple images and a good accuracy in their reproduced positions.

⁸ <https://archive.stsci.edu/prepds/frontier/lensmodels/>

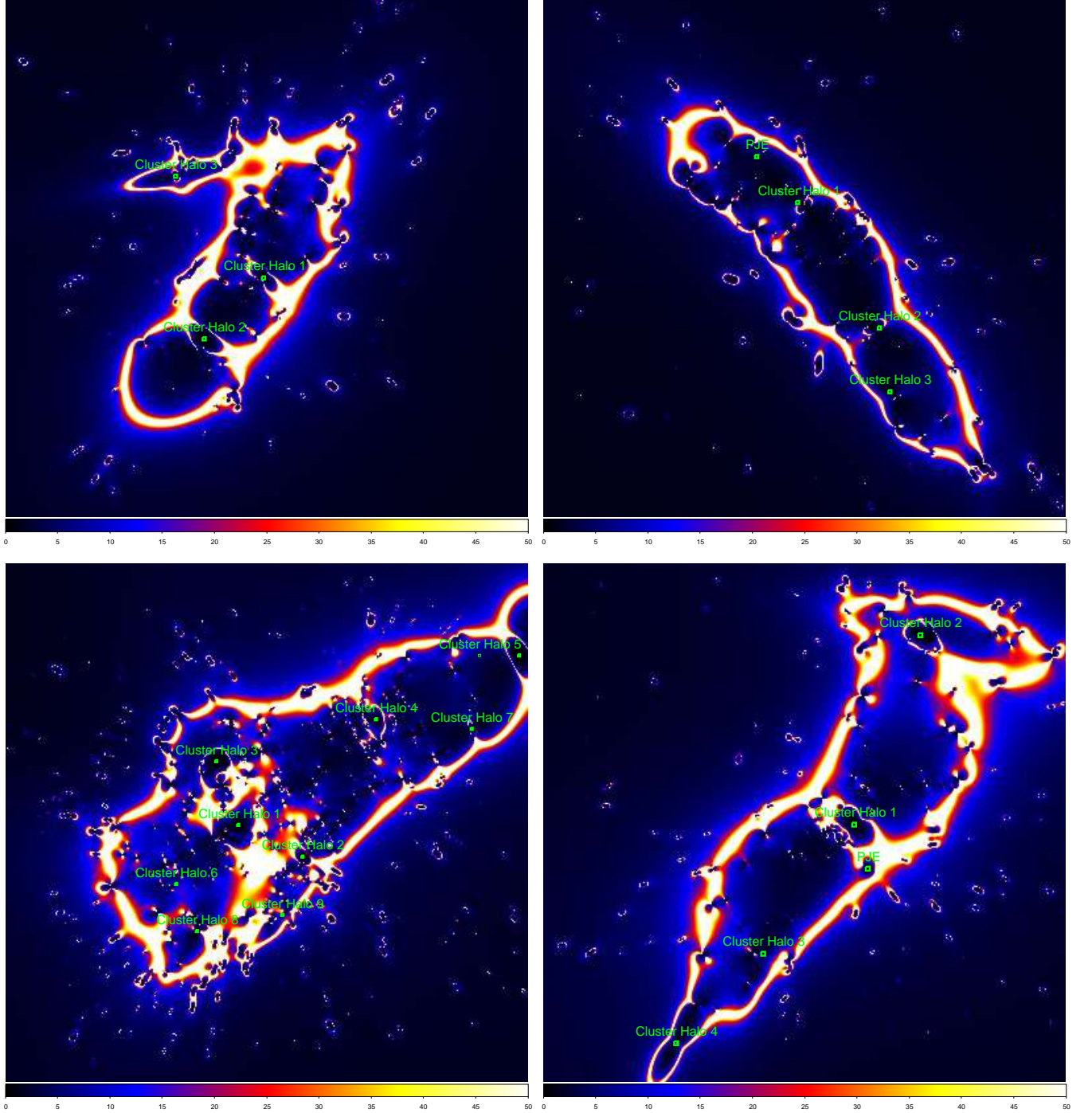


Figure 3. Positions of model components are shown on a magnification map for $z = 9$ sources for Abell 2744 (*upper left*), MACS J0416.1–2403 (*upper right*), MACS J0717.5+3745 (*lower left*), and MACS J1149.6+2223 (*lower right*).

To illustrate this point further, in Figure 4 we plot the distributions of $\Delta_x \equiv |\mathbf{x}_{\text{obs}} - \mathbf{x}_{\text{model}}|$, the distance between the observed and model-predicted image positions for each multiple image. We find that for any cluster Δ_x is indeed small for most of the multiple images, with a distribution peaking around $0''.2$ and most multiple images having $\Delta_x < 0''.6$, which again indicates the success of our mass modeling.

The accuracy of our mass models may be tested further by observations of other than image positions. For Abell 2744, our model yields a magnification $\mu = 2.26 \pm 0.12$ at

the position of the lensed Type Ia supernova HFF14Tom (Rodney et al. 2015a). This is fully consistent with the observed magnification $\mu = 2.03 \pm 0.29$, although we note that this may not be a fair comparison as we have explicitly included the observed magnification as a constraint in mass modeling. On the other hand, the time delays and flux ratios of the lensed supernova SN Refsdal (Kelly et al. 2015b) in MACS J1149.6+2223 can provide a useful blind test of our mass model. We will discuss this blind test in Section 4.3.

As shown in Tables 2–5, some NFW components have

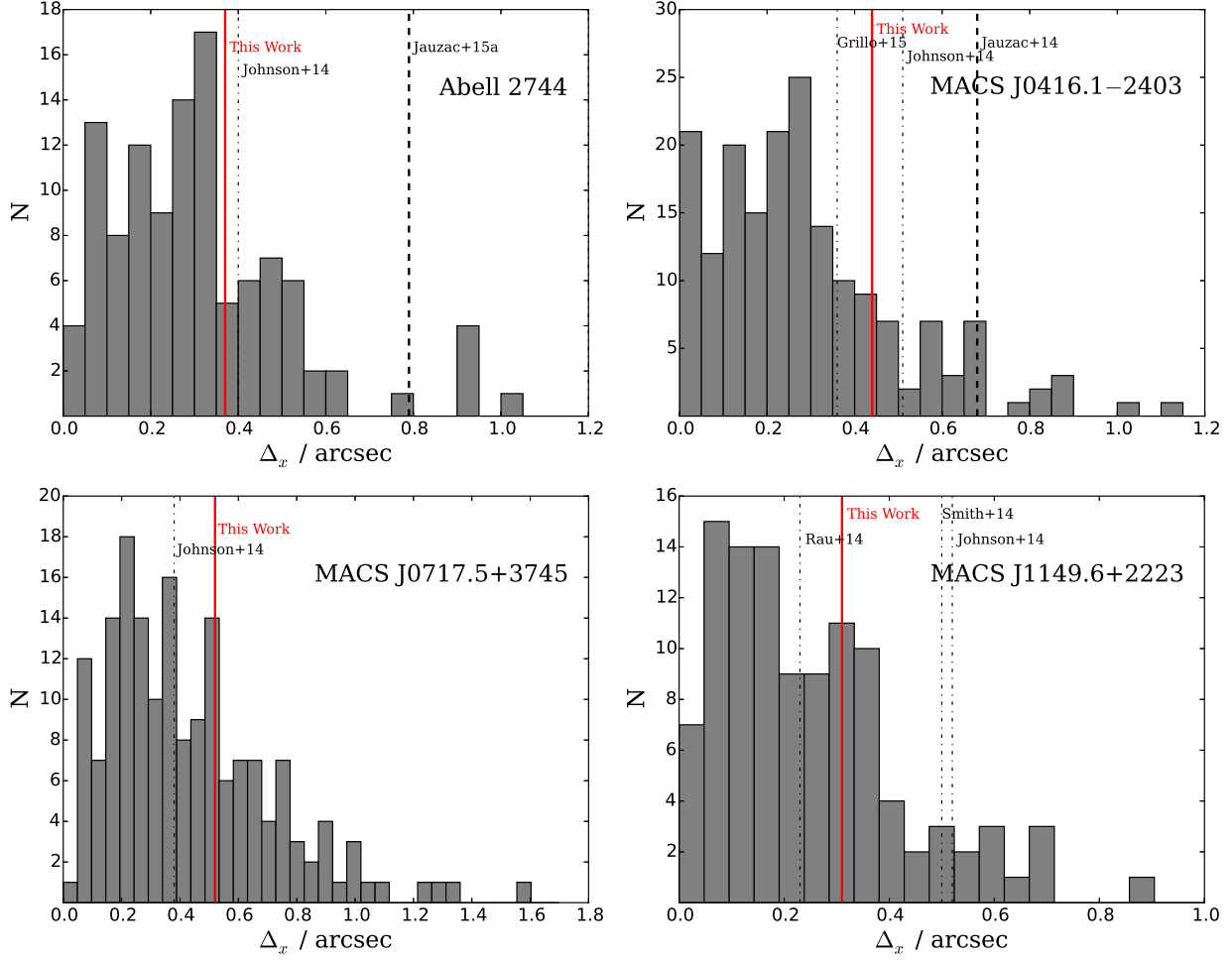


Figure 4. The distribution of the distances between observed and model-predicted image positions, $\Delta_x \equiv |\mathbf{x}_{\text{obs}} - \mathbf{x}_{\text{model}}|$, for all the multiple images used for mass modeling for Abell 2744 (*upper left*), MACS J0416.1–2403 (*upper right*), MACS J0717.5+3745 (*lower left*), and MACS J1149.6+2223 (*lower right*). See Appendix A for lists of multiple images for individual clusters. The red solid, black long-dashed, and black dash-dotted vertical lines show RMSs of Δ_x calculated from our models, previous mass models that used more than 100 multiple images, and previous mass models that used less than 100 multiple images, respectively. The RMSs of Δ_x for all the clusters are summarized in Table 1.

high ellipticities ($e > 0.7$). There are presumably two reasons for this. The first reason is that the intrinsic mass distribution is indeed highly elongated, which is not surprising given the axis-ratio distribution of simulated dark matter halos (e.g., Jing & Suto 2002). In some cases, such as Cluster halos 2 and 9 in MACS J0717.5+3745, such a high elongation is also implied by aligned positions of nearby member galaxies. The second reason may be an insufficient number of multiple images around the position of the NFW component. If multiple images are unevenly distributed around an NFW component, the model parameters can sometimes be biased toward the local potential, around where the multiple images are observed. This is the case for Cluster halo 3 in the Abell 2744 field and Cluster halo 8 in the MACS J0717.5+3745 field. In the case of Cluster halo 3 in the Abell 2744 field, an additional NFW component is required besides the GALs component so that the positions of the multiple images located 20 arcsec southwest are well reproduced. However, this component is optimized to have a higher ellipticity than the actual galaxy light distribution presumably because of the small number of multiple images around it to constrain its parameters.

4.2. Model comparison

Some teams have also constructed precise mass models exploiting the full-depth HFF data and more than 100 multiple images. We here compare our best-fitting mass models with those obtained in previous work.

Abell 2744 — We place three cluster-scale NFW components to model the cluster mass distribution. The positions of Cluster halos 1 and 2 are consistent with those in Jauzac et al. (2015a). Wang et al. (2015), who adopt a free-form modeling method, also predict mass peaks at these positions. In addition, we assume a third NFW component, Cluster halo 3, as described above, where there is also a mass peak in Wang et al.’s (2015) model.

MACS J0416.1–2403 — We place three cluster-scale NFW components and one PJE component. The PJE component is for better modeling of the member galaxy near systems 1, 2, 6, 89, and 90, as this member has a significant effect on these multiple image systems. The positions of Cluster halos 1 and 2 are consistent with those in Jauzac et al. (2014) and Diego et al. (2015a), but the PJE component is included only in our model. While Jauzac et al. (2014) and Diego et al. (2015a) assume only two halo components, there is a “soft compo-

ment” in the model of Diego et al. (2015a) at the position of our Cluster halo 3.

MACS J0717.5+3745 — Limousin et al. (2015) use four halo-scale profiles. Diego et al. (2015b) also identify four mass peaks in their free-form model. While we place nine cluster-scale NFW components, only four, Cluster halos 1+3, 2, 4, and 5, have a significant mass peak. This is consistent with their results. Limousin et al. (2015) report very shallow mass profiles for this cluster, which is consistent with our NFW components having relatively smaller concentration parameters. We note that the position of Cluster halo 9 is consistent with an X-ray emission peak from *Chandra* (see Figure 4 in Diego et al. 2015b).

MACS J1149.6+2223 — We place four cluster-scale NFW components and one PJE component. The positions of Cluster halos 1, 2, and 3 are consistent with those in Jauzac et al. (2015b). They do not place a component at the position of Cluster halo 4. On the other hand, they place a halo component at the position of a bright member galaxy located ~ 100 arcsec north from the BCG and is out of the region of the HFF WFC3/IR observation.

4.3. Predictions for SN Refsdal

In our mass modeling of MACS J1149.6+2223, we only use positions of the multiple images S1–S4 of SN Refsdal as observational constraints. Importantly, when our mass modeling was completed, any relative time delays and magnifications had not been measured yet, which indicates that observations of relative time delays and magnifications serve as an important *blind* test of our mass model. Treu et al. (2015a) made a detailed comparison of predictions of our best-fitting model (corresponding to the short name “Ogu-a” in Treu et al. 2015a) with those from other mass modeling teams. Treu et al. (2015a) also compared predictions of relative magnifications and time delays between images S1–S4 with preliminary measurements, finding a good agreement between our best-fit model predictions and observations. Updated measurements and comparisons are available in Rodney et al. (2015b).

Most mass models of MACS J1149.6+2223 predict two additional images of SN Refsdal around images 1.2 and 1.3, which we call SX and SY following Oguri (2015). SX is predicted to appear approximately one year after S1–S4, whereas SY is predicted to have appeared a decade ago. Our refined model predictions for the time delay, position, and magnification factor of SX are $\Delta t_{\text{SX}} = 336^{+22}_{-20}$ days, $x_{\text{SX}} = -4.16^{+0.08}_{-0.07}$ arcsec, $y_{\text{SX}} = -6.50^{+0.08}_{-0.08}$ arcsec, and $\mu_{\text{SX}} = 4.23^{+0.32}_{-0.31}$, where Δt_{SX} is the relative time delay from the image S1, x_{SX} and y_{SX} are coordinates relative to the BCG. The predicted time delay, position, and magnification factor of SY are $\Delta t_{\text{SY}} = -6229^{+209}_{-227}$ days, $x_{\text{SY}} = -16.7^{+0.08}_{-0.08}$ arcsec, $y_{\text{SY}} = 12.8^{+0.12}_{-0.12}$ arcsec, and $\mu_{\text{SY}} = 3.52^{+0.19}_{-0.17}$.

While this paper is under review, a new SN image was discovered in *HST* images taken on 11 December (Kelly et al. 2015a). The observed position of the image is $x = -4.43$ arcsec and $y = -6.62$ arcsec, which is fully consistent with the predicted position of SX with offsets from the predicted position only 0.27 arcsec to the east and 0.12 arcsec to the south. Furthermore, as can be

seen in Figure 2 in Kelly et al. (2015a), our time delay and magnification predictions on SX are fully consistent with the observed values. We again emphasize that these predictions are made before the reappearance of the new image. These blind test results support the validity and accuracy of our mass modeling method.

5. DROPOUT GALAXY SAMPLE

5.1. Lyman Break Galaxy Selection

Galaxies at $z \sim 6-7$ are selected by the Lyman break technique with the continuum spectral break falling in the i_{814} band. We adopt the selection criteria used in Atek et al. (2015a)

$$i_{814} - Y_{105} > 0.8, \quad (4)$$

$$Y_{105} - J_{125} < 0.8, \quad (5)$$

$$i_{814} - Y_{105} > 2(Y_{105} - J_{125}) + 0.6. \quad (6)$$

Objects which show 2σ level signals in both the B_{435} and V_{606} band images or in the $B_{435}+V_{606}$ stacked image are excluded. We require that objects need to be detected at the 5σ level both in the Y_{105} and J_{125} bands. For an object not detected in the i_{814} band, we calculate the $i_{814} - Y_{105}$ color assigning the 2σ limiting magnitude to the i_{814} band magnitude.

To select galaxies at $z \sim 8$, we adopt the selection criteria presented in Atek et al. (2014)

$$Y_{105} - J_{125} > 0.5, \quad (7)$$

$$J_{125} - JH_{140} < 0.5, \quad (8)$$

$$Y_{105} - J_{125} > 0.4 + 1.6(J_{125} - JH_{140}). \quad (9)$$

Objects which show a 2σ level signal in at least one of the B_{435} , V_{606} , or i_{814} band image are excluded. Again, objects also need to be detected at the 5σ level in all the J_{125} , JH_{140} , and H_{160} band images.

To select galaxies at $z \sim 9$, we adopt the selection criteria similar to those presented in Ishigaki et al. (2015)

$$(Y_{105} + J_{125})/2 - JH_{140} > 0.75, \quad (10)$$

$$(Y_{105} + J_{125})/2 - JH_{140} > 0.75 + 0.8(JH_{140} - H_{160}), \quad (11)$$

$$J_{125} - H_{160} < 1.15, \quad (12)$$

$$JH_{140} - H_{160} < 0.6. \quad (13)$$

Objects which show a 2σ level signal in at least one of the B_{435} , V_{606} , or i_{814} band image are excluded. We require that objects need to be detected at the 3σ level in both the JH_{140} and H_{160} band images and at the 3.5σ level in at least one of these two bands. If an object is fainter than the 0.9σ level magnitude in the Y_{105} or J_{125} band, we assign the 0.9σ level magnitude to the photometry of that band.

In addition, we adopt a pseudo- χ^2 constraint to reduce the contamination rate. This constraint is defined as $\chi^2_{\text{opt}} < 2.8$, where $\chi^2_{\text{opt}} = \sum_i \text{SGN}(f_i)(f_i/\sigma_i)^2$. Here, f_i is the flux density in the i -th band and $\text{SGN}(x)$ is the sign function defined by $\text{SGN}(x) = 1$ if $x > 0$ and $\text{SGN}(x) = -1$ if $x < 0$. The summation runs over all the optical bands. Finally, we visually inspect all the dropout galaxy candidates and remove seven obvious spurious sources.

5.2. Dropout galaxy sample

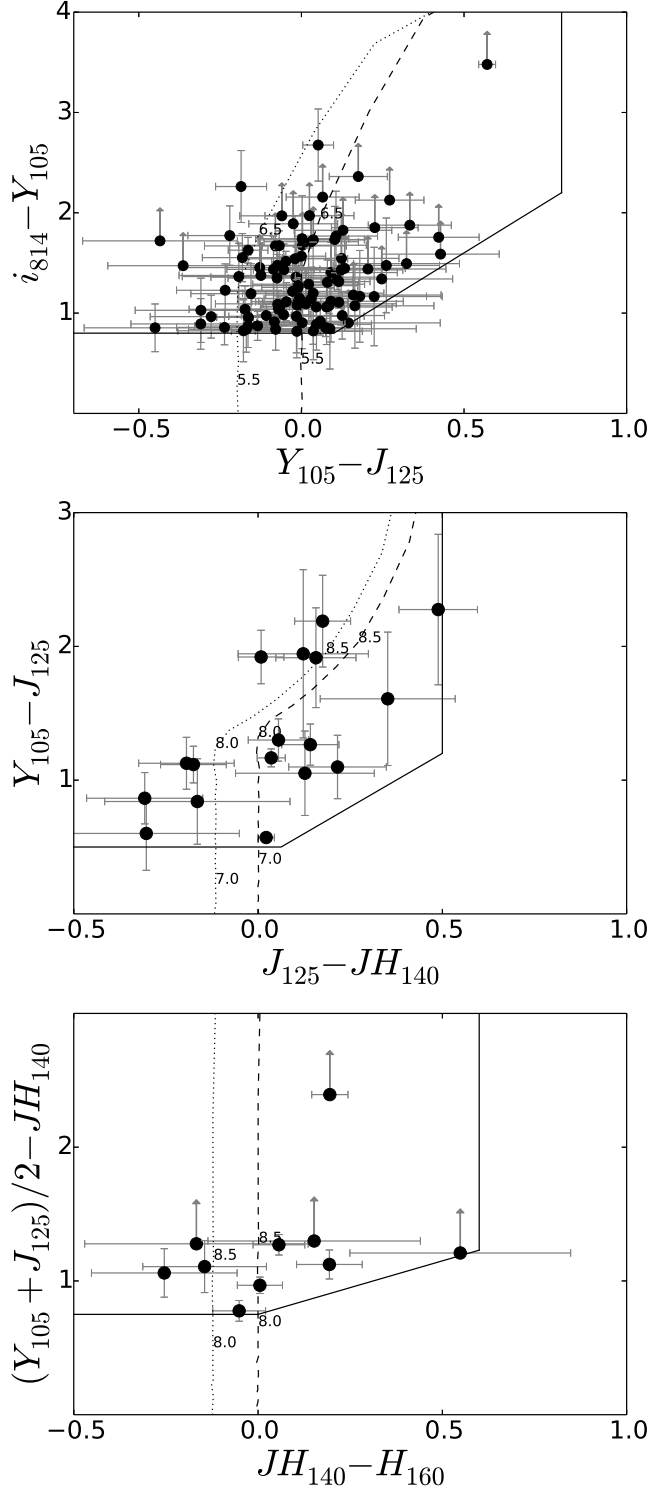


Figure 5. Two-color diagrams for *i*-dropout (top), *Y*-dropout (middle), and *YJ*-dropout (bottom) galaxy candidates, with our color selections indicated with solid lines. Filled circles represent dropout galaxy candidates. Tracks of expected galaxy colors computed assuming UV-slopes of $\beta = -2$ and -3 are shown with dashed and dotted lines, respectively. Small numbers represent assumed redshifts. The colors of all the dropout galaxy candidates are summarized in Tables B1–B3.

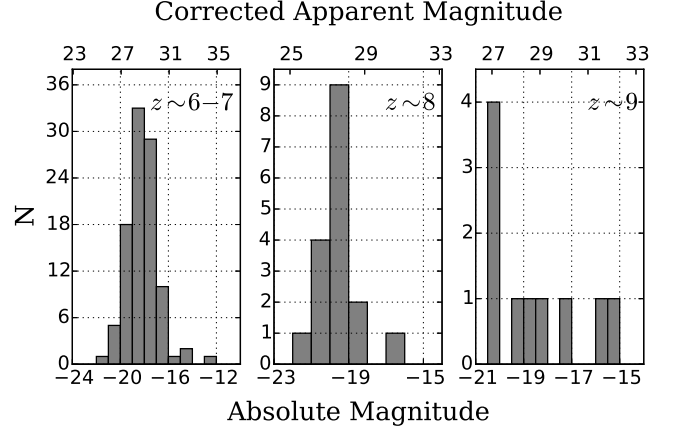


Figure 6. Histograms of dropout galaxies at $z \sim 6-7$ (left panel), $z \sim 8$ (middle panel), and $z \sim 9$ (right panel) in the four HFF cluster fields as a function of the intrinsic (unlensed) absolute magnitude. Magnification factors of individual dropout galaxies are corrected based on our best-fitting mass models. Most of the intrinsically faint galaxies are highly magnified and their estimated magnitudes are affected by the uncertainty in the magnification factor. Nevertheless, magnitude errors propagated from errors in the magnification factor in the $z \sim 6-7$, 8, and 9 samples are no larger than only 0.87, 0.11, and 1.19 mag, respectively. Details of these dropout galaxies are given in Tables B1–B3. Note that all of the dropout galaxy candidates are plotted here.

We list the *i*-dropout ($z \sim 6-7$), *Y*-dropout ($z \sim 8$), and *YJ*-dropout ($z \sim 9$) galaxies from the four HFF cluster fields in Tables B1–B3 respectively in Appendix B. We show the distribution of these dropout galaxies in color-color spaces in Figure 5. For each galaxy, the first part of ID represents the field in which it is found; 1C, 2C, 3C, and 4C indicate Abell 2744 cluster, MACS J0416.1–2403 cluster, MACS J0717.5+3745 cluster, and MACS J1149.6+2223 cluster fields, respectively. The second part of ID represents its coordinates.⁹ In the Tables we also provide magnification factors at the positions of galaxies predicted by our mass models presented in Section 4.

In summary, we select 100 *i*-dropout, 17 *Y*-dropout, and 10 *YJ*-dropout galaxies. Note that there are some overlaps in the dropout samples. We find that one object is identified by the *Y*- and *i*-dropout selections, and that six objects meet the criteria of the *YJ*- and *Y*-dropout selections. Most of the dropout galaxies have a modest magnification factor, $\mu \lesssim 5$, while some are highly magnified. For instance, based on the magnification maps of our best-fitting models, 14 and four galaxies at $z \sim 6-7$ and 9, respectively, have a magnification factor larger than 10. Among them four at $z \sim 6-7$ and one at $z \sim 9$ have a magnification factor larger than 50, albeit with large uncertainties.

Some of these high-magnification galaxies may be intrinsically faint. To examine this possibility, we plot the histograms of all dropout galaxies as a function of intrinsic magnitude corrected for magnification factor in Figure 6. We find that they typically have absolute magnitudes of $M_{UV} \sim -18$, or intrinsic magnitude of ~ 29 mag, but some are as faint as $M_{UV} \sim -14$, or intrinsic magnitude of ~ 33 mag.

⁹ For example, HFF1C-2251-4556 is found in Abell 2744 cluster field and its coordinates are R.A.=00:14:22.51, Decl.=−30:24:55.6.

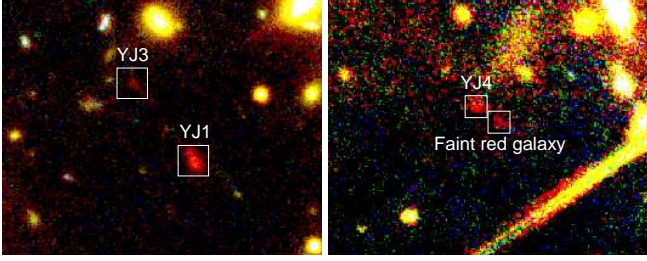


Figure 7. Color-composite images of the multiple image candidates, HFF4C-YJ1 and HFF4C-YJ3 (*left panel*), and of HFF4C-YJ4 and its companion (*right panel*). *Left:* HFF4C-YJ1 and HFF4C-YJ3 may be distorted in the direction of the shear at that position. *Right:* A faint red galaxy is located very close to HFF4C-YJ4, and its position is consistent with being a counter image of HFF4C-YJ4.

5.3. Multiple image candidates

Our analysis suggests that some dropout galaxies are multiply imaged. Among them, reliable ones have been included in our mass modeling; systems 28, 46, and 54 in Abell 2744 field; systems 6, 90, 91, and 92 in MACS J0416.1–2403 field; systems 19 and 66 in MACS J0717.5+3745 field; and systems 33, 38, and 39 in MACS J1149.6+2223 field (see Section 4). Here we discuss several interesting reliable multiple images and multiple image candidates at $z \sim 9$.

HFF2C-i2, -i3, -i7, and -i16 — These are newly identified multiple images in MACS J0416.1–2403 field. HFF2C-i2 and -i16 compose system 91, and HFF2C-i3 and -i7 compose system 92. They are placed in the most northeast part of this cluster and improve mass modeling in this region.

HFF4C-YJ1 and HFF4C-YJ3 — HFF4C-YJ1 is a bright $z \sim 9$ galaxy candidate in MACS J1149.6+2223 discovered by Zheng et al. (2012). We find a faint $z \sim 9$ galaxy candidate, HFF4C-YJ3, close to this galaxy (see Figures 2 and 7). Our best-fitting mass model has a critical curve that is placed near these galaxies. Therefore, it is possible that these two galaxies are in fact multiple images of a $z \sim 9$ galaxy. The reliability of this multiple image system is not very high, because there are not many known multiple images around this system, and therefore our mass model in this region includes relatively large uncertainties. The $JH_{140} - H_{160}$ colors of YJ1 and YJ3 are 0.24 ± 0.04 and 0.16 ± 0.23 , respectively, and are consistent with being multiple images.

HFF4C-YJ4 — This is a $z \sim 9$ galaxy in MACS J1149.6+2223 near the critical curve. We find another faint red galaxy nearby this galaxy (see Figure 7). The color of this faint red galaxy is consistent with being at $z \sim 9$, but it is below the detection limit used for the dropout selection. The relative positions of these two galaxies are fully consistent with being multiple images of a single $z \sim 9$ galaxy. Given its high reliability, we include the positions of these galaxies as constraints in our mass modeling as system 38. The $JH_{140} - H_{160}$ colors of YJ4 and the faint red galaxy are -0.15 ± 0.24 and 0.19 ± 0.24 , respectively. This is consistent with being multiple images.

Even if these galaxy pairs are not real multiple images of single galaxies, the close separations are interesting in term of galaxy formation and evolution.

5.4. Future Analyses

We have presented a sample of high-redshift galaxies selected in the cluster fields where lensing effects are significant. If those from the accompanied parallel fields are added, we will have a four times larger sample of $z \gtrsim 6$ galaxies than that used in our previous studies (Ishigaki et al. 2015; Kawamata et al. 2015). In the forthcoming papers, we plan to use this large sample to investigate various properties of high-redshift galaxies including luminosity functions, sizes and morphologies, and stellar populations, and their implications for cosmic reionization.

The absolute magnitudes of the new high-redshift galaxy sample constructed in this paper extend down to $M_{UV} \simeq -12.1$, -16.8 , and -15.0 at $z \sim 6-7$, 8 , and 9 , respectively, enabling us to study extremely faint galaxies in the reionization era. These limiting magnitudes at $z \sim 6-7$ and 9 are significantly fainter than those in previous studies based on only one or two clusters (e.g., $M_{UV} \simeq -15.25$ at $z \sim 6-7$ in Atek et al. 2015b and $M_{UV} \simeq -18.1$ at $z \sim 9$ in McLeod et al. 2015).

6. CONCLUSION

We have conducted precise mass modeling of four HFF clusters, exploiting the full depth HFF data and the latest spectroscopic follow-up results on multiple images. We have used the positions of 111, 182, 173, and 108 multiple images to constrain the matter distributions of Abell 2744, MACS J0416.1–2403, MACS J0717.5+3745, and MACS J1149.6+2223, respectively. Among them, 145 multiple images are new systems identified in this paper. We assume simply parametrized mass models and optimize model parameters with the public software GLAFIC (Oguri 2010). We have found that our best-fitting mass models reproduce the observed positions of multiple images quite well, with image plane RMS of $\sim 0''.4$ (see Table 1). For Abell 2744, our best-fitting mass model recovers the observed magnification at the position of the Type Ia supernova HFF14Tom (Rodney et al. 2015a), although we note that we have explicitly included this magnification as a constraint in mass modeling. We have found that the predicted time delays and flux ratios of the quadruple images of SN Refsdal (Kelly et al. 2015b) in MACS J1149.6+2223 are consistent with observations (Treu et al. 2015a).

We have then constructed $z \sim 6-9$ dropout galaxy catalogs in these four cluster fields from the full depth HFF images. For each dropout galaxy we have estimated the magnification factor from our mass modeling results. The catalogs consist of 100 galaxies at $z \sim 6-7$, 17 galaxies at $z \sim 8$, and 10 galaxies at $z \sim 9$, although some of them are detected in multiple dropout selections. While most of these galaxies have modest magnifications, $\mu \lesssim 5$, there are several dropout galaxies with a magnification larger than 10. Specifically, 14 at $z \sim 6-7$ and four at $z \sim 9$ have a predicted magnification factor larger than 10. The intrinsic (unlensed) magnitudes of these high-magnification galaxies are estimated to be $\sim 32-33$ mag, which indicates that the HFF program indeed detects the faintest galaxies known to date.

ACKNOWLEDGMENTS

We thank the Frontier Fields mass modeling initiative led by Dan Coe and participants of this initiative for sharing invaluable data before the publications. We are

grateful to the authors of Treu et al. (2015a) for sharing the follow-up data of MACS J1149.6+2223 and for helpful discussions. This work was supported in part by World Premier International Research Center Initiative (WPI Initiative), MEXT, Japan, and JSPS KAKENHI Grant Number 26800093, 23244025, 15H05892, and 15H02064.

REFERENCES

- Abell, G. O. 1958, *ApJS*, 3, 211
Atek, H., Richard, J., Kneib, J.-P., et al. 2014, *ApJ*, 786, 60
—, 2015a, *ApJ*, 800, 18
Atek, H., Richard, J., Jauzac, M., et al. 2015b, *ArXiv e-prints*, arXiv:1509.06764
Benítez, N. 2000, *ApJ*, 536, 571
Bertin, E., & Arnouts, S. 1996, *A&AS*, 117, 393
Bertin, E., Mellier, Y., Radovich, M., et al. 2002, in *Astronomical Society of the Pacific Conference Series*, Vol. 281, *Astronomical Data Analysis Software and Systems XI*, ed. D. A. Bohlender, D. Durand, & T. H. Handley, 228
Bradley, L. D., Zitrin, A., Coe, D., et al. 2014, *ApJ*, 792, 76
Broadhurst, T., Benítez, N., Coe, D., et al. 2005, *ApJ*, 621, 53
Christensen, L., Richard, J., Hjorth, J., et al. 2012, *MNRAS*, 427, 1953
Coe, D., Bradley, L., & Zitrin, A. 2015, *ApJ*, 800, 84
Diego, J. M., Broadhurst, T., Molnar, S. M., Lam, D., & Lim, J. 2015a, *MNRAS*, 447, 3130
Diego, J. M., Broadhurst, T., Zitrin, A., et al. 2015b, *MNRAS*, 451, 3920
Diego, J. M., Broadhurst, T., Chen, C., et al. 2015c, *ArXiv e-prints*, arXiv:1504.05953
Ebeling, H., Barrett, E., Donovan, D., et al. 2007, *ApJ*, 661, L33
Ebeling, H., Ma, C.-J., & Barrett, E. 2014, *ApJS*, 211, 21
Grillo, C., Suyu, S. H., Rosati, P., et al. 2015a, *ApJ*, 800, 38
Grillo, C., Karman, W., Suyu, S. H., et al. 2015b, *ArXiv e-prints*, arXiv:1511.04093
Ishigaki, M., Kawamata, R., Ouchi, M., et al. 2015, *ApJ*, 799, 12
Jauzac, M., Clément, B., Limousin, M., et al. 2014, *MNRAS*, 443, 1549
Jauzac, M., Richard, J., Jullo, E., et al. 2015a, *MNRAS*, 452, 1437
Jauzac, M., Richard, J., Limousin, M., et al. 2015b, *ArXiv e-prints*, arXiv:1509.08914
Jing, Y. P., & Suto, Y. 2002, *ApJ*, 574, 538
Johnson, T. L., Sharon, K., Bayliss, M. B., et al. 2014, *ApJ*, 797, 48
Karman, W., Caputi, K. I., Grillo, C., et al. 2015, *A&A*, 574, A11
Kawamata, R., Ishigaki, M., Shimasaku, K., Oguri, M., & Ouchi, M. 2015, *ApJ*, 804, 103
Keeton, C. R. 2001, *ArXiv Astrophysics e-prints*, astro-ph/0102341
Kelly, P. L., Rodney, S. A., Treu, T., et al. 2015a, *ArXiv e-prints*, arXiv:1512.04654
—, 2015b, *Science*, 347, 1123
Köhlinger, F., & Schmidt, R. W. 2014, *MNRAS*, 437, 1858
Lam, D., Broadhurst, T., Diego, J. M., et al. 2014, *ApJ*, 797, 98
Laporte, N., Streblyanska, A., Clement, B., et al. 2014, *A&A*, 562, L8
Laporte, N., Streblyanska, A., Kim, S., et al. 2015, *A&A*, 575, A92
Limousin, M., Ebeling, H., Richard, J., et al. 2012, *A&A*, 544, A71
Limousin, M., Richard, J., Jullo, E., et al. 2015, *ArXiv e-prints*, arXiv:1510.08077
Mann, A. W., & Ebeling, H. 2012, *MNRAS*, 420, 2120
McLeod, D. J., McLure, R. J., Dunlop, J. S., et al. 2015, *MNRAS*, 450, 3032
Merten, J., Coe, D., Dupke, R., et al. 2011, *MNRAS*, 417, 333
Navarro, J. F., Frenk, C. S., & White, S. D. M. 1997, *ApJ*, 490, 493
Newman, A. B., Ellis, R. S., & Treu, T. 2015, *ArXiv e-prints*, arXiv:1503.05282
Oesch, P. A., Bouwens, R. J., Illingworth, G. D., et al. 2015, *ApJ*, 808, 104
Oguri, M. 2010, *PASJ*, 62, 1017
—, 2015, *MNRAS*, 449, L86
Oguri, M., Bayliss, M. B., Dahle, H., et al. 2012, *MNRAS*, 420, 3213
Oguri, M., Schrabback, T., Jullo, E., et al. 2013, *MNRAS*, 429, 482
Oke, J. B., & Gunn, J. E. 1983, *ApJ*, 266, 713
Owers, M. S., Randall, S. W., Nulsen, P. E. J., et al. 2011, *ApJ*, 728, 27
Postman, M., Coe, D., Benítez, N., et al. 2012, *ApJS*, 199, 25
Rau, S., Vegetti, S., & White, S. D. M. 2014, *MNRAS*, 443, 957
Richard, J., Jauzac, M., Limousin, M., et al. 2014, *MNRAS*, 444, 268
Rodney, S. A., Patel, B., Scolnic, D., et al. 2015a, *ApJ*, 811, 70
Rodney, S. A., Strolger, L.-G., Kelly, P. L., et al. 2015b, *ArXiv e-prints*, arXiv:1512.05734
Schmidt, K. B., Treu, T., Brammer, G. B., et al. 2014, *ApJ*, 782, L36
Schneider, P., Ehlers, J., & Falco, E. E. 1992, *Gravitational Lenses*
Schramm, T. 1990, *A&A*, 231, 19
Sebesta, K., Williams, L. L. R., Mohammed, I., Saha, P., & Liesenborgs, J. 2015, *ArXiv e-prints*, arXiv:1507.08960
Sharon, K., & Johnson, T. L. 2015, *ApJ*, 800, L26
Smith, G. P., Ebeling, H., Limousin, M., et al. 2009, *ApJ*, 707, L163
Treu, T., Brammer, G., Diego, J. M., et al. 2015a, *ArXiv e-prints*, arXiv:1510.05750
Treu, T., Schmidt, K. B., Brammer, G. B., et al. 2015b, *ArXiv e-prints*, arXiv:1509.00475
Vanzella, E., Fontana, A., Zitrin, A., et al. 2014, *ApJ*, 783, L12
Wang, X., Hoag, A., Huang, K.-H., et al. 2015, *ApJ*, 811, 29
Zheng, W., Postman, M., Zitrin, A., et al. 2012, *Nature*, 489, 406
Zheng, W., Shu, X., Moustakas, J., et al. 2014, *ArXiv e-prints*, arXiv:1402.6743
Zitrin, A., & Broadhurst, T. 2009, *ApJ*, 703, L132
Zitrin, A., Broadhurst, T., Rephaeli, Y., & Sadeh, S. 2009, *ApJ*, 707, L102
Zitrin, A., Ellis, R. S., Belli, S., & Stark, D. P. 2015a, *ApJ*, 805, L7
Zitrin, A., Meneghetti, M., Umetsu, K., et al. 2013, *ApJ*, 762, L30
Zitrin, A., Zheng, W., Broadhurst, T., et al. 2014, *ApJ*, 793, L12
Zitrin, A., Fabris, A., Merten, J., et al. 2015b, *ApJ*, 801, 44

APPENDIX

A. LISTS OF MULTIPLE IMAGES USED FOR MASS MODELING

The list of multiple images we use for mass modeling is given in Tables A1–A4.

Table A1
Abell 2744 Multiple Image Systems

ID	R.A.	Decl.	z_{spec}	z_{model}	Photo-z prior	Reference ^a
1.1	3.597542	−30.403917	1.500	JM, XW
1.2	3.595958	−30.406822		JM
1.3	3.586208	−30.409986		JM
2.1	3.583250	−30.403350	...	$1.89^{+0.07}_{-0.07}$...	JM

Table A1 — *Continued*

ID	R.A.	Decl.	z_{spec}	z_{model}	Photo-z prior	Reference ^a
2.2	3.597292	−30.396725	JM
2.3	3.585417	−30.399897	JM
2.4	3.586417	−30.402128	JM
3.1	3.589480	−30.393867	3.980	JM, TJ
3.2	3.588647	−30.393788		JM
4.1	3.592125	−30.402633	3.580	JM, JR
4.2	3.595625	−30.401622		JM
4.3	3.580417	−30.408925		JM
4.4	3.593208	−30.404914		JR
4.5	3.593583	−30.405106		JR
5.1	3.583417	−30.392069	...	$1.94^{+0.12}_{-0.11}$...	JM
5.2	3.585000	−30.391375	JM
5.3	3.579959	−30.394761	JM
5.4	3.582292	−30.392784
6.1	3.598535	−30.401797	2.019	JM, JR
6.2	3.594042	−30.408011		JM
6.3	3.586417	−30.409372		JM
7.1	3.598261	−30.402322	...	$2.50^{+0.14}_{-0.12}$	3.25 ± 0.5	JM
7.2	3.595233	−30.407407	...			JM
7.3	3.584601	−30.409818	...			JM
8.1	3.589708	−30.394339	...	$4.22^{+0.45}_{-0.35}$...	JM
8.2	3.588834	−30.394222	JM
8.3	3.576389	−30.402559	MJ
9.1	3.588375	−30.405272	...	$2.31^{+0.52}_{-0.33}$...	JM
9.2	3.587125	−30.406242	JM
10.1	3.588417	−30.405878	...	$3.47^{+0.35}_{-0.34}$	2.86 ± 0.5	JM
10.2	3.587375	−30.406481	...			JM
11.1	3.591375	−30.403858	...	$2.56^{+0.13}_{-0.12}$...	JM
11.2	3.597264	−30.401431	JM
11.3	3.582792	−30.408914	JM
11.4	3.594542	−30.406542	JR
12.2	3.593239	−30.403249	...	$3.05^{+0.39}_{-0.33}$	2.80 ± 0.5	JR
12.3	3.594555	−30.402996	...			JR
13.1	3.592375	−30.402558	...	$1.42^{+0.05}_{-0.04}$...	JR
13.2	3.593792	−30.402164	JR
13.3	3.582792	−30.408044	JR
14.1	3.589750	−30.394636	...	$2.34^{+0.12}_{-0.11}$...	JR
14.2	3.588458	−30.394436	JR
14.3	3.577577	−30.401682	MJ
18.1	3.590750	−30.395561	5.660	JR, XW
18.2	3.588375	−30.395636		JR
18.3	3.576123	−30.404489		DL
20.1	3.596234	−30.402976	...	$2.58^{+0.13}_{-0.12}$...	DL
20.2	3.595172	−30.405442	DL
20.3	3.581992	−30.409550	MJ
21.1	3.596176	−30.403117	...	$2.58^{+0.12}_{-0.12}$...	DL
21.2	3.595259	−30.405342	DL
21.3	3.581973	−30.409600	MJ
22.1	3.587919	−30.411613	...	$3.26^{+0.27}_{-0.22}$...	DL
22.2	3.600059	−30.404395	HA14
22.3	3.596572	−30.409000	HA14
23.1	3.588157	−30.410550	...	$3.40^{+0.24}_{-0.23}$...	DL
23.2	3.593552	−30.409709	HA14
23.3	3.600541	−30.401816	HA14
24.1	3.595902	−30.404467	...	$1.02^{+0.03}_{-0.03}$...	MJ
24.2	3.595114	−30.405909	MJ
24.3	3.587332	−30.409095	MJ
25.1	3.594476	−30.402742	...	$1.21^{+0.04}_{-0.03}$...	MJ
25.2	3.592147	−30.403317	MJ
25.3	3.584215	−30.408284	MJ
26.1	3.593906	−30.409726	...	$2.38^{+0.12}_{-0.11}$...	DL
26.2	3.590350	−30.410584	DL
26.3	3.600099	−30.402976	DL
28.1	3.580452	−30.405043	...	$6.40^{+0.38}_{-0.39}$	6.70 ± 0.5	HA14
28.2	3.597831	−30.395958	...			HA14
28.3	3.585321	−30.397958	...			HA14
28.4	3.587442	−30.401376	...			DL
29.1	3.582437	−30.397575	...	$2.63^{+0.30}_{-0.25}$...	MJ
29.2	3.580524	−30.400475	MJ
30.1	3.591016	−30.397439	...	$0.97^{+0.03}_{-0.02}$	0.85 ± 0.5	MJ
30.2	3.586669	−30.398184	...			MJ

Table A1 — *Continued*

ID	R.A.	Decl.	z_{spec}	z_{model}	Photo-z prior	Reference ^a
30.3	3.581923	−30.401704	...			MJ
31.1	3.585925	−30.403159	...	$5.31^{+1.86}_{-1.02}$...	DL
31.2	3.583703	−30.404100	DL
32.1	3.583605	−30.404712	...	$4.03^{+0.38}_{-0.31}$...	MJ
32.2	3.586667	−30.403337	MJ
32.3	3.599789	−30.395980	MJ
33.1	3.584698	−30.403150	...	$4.86^{+0.57}_{-0.43}$...	HA14
33.2	3.584389	−30.403401	HA14
33.3	3.600649	−30.395425	MJ
34.1	3.593427	−30.410847	...	$2.54^{+0.19}_{-0.17}$...	MJ
34.2	3.593813	−30.410723	MJ
34.3	3.600585	−30.404477	MJ
41.1	3.599161	−30.399592	...	$4.57^{+0.49}_{-0.40}$...	MJ
41.3	3.583451	−30.408506	MJ
46.1	3.595007	−30.400759	...	$9.79^{+0.45}_{-0.44}$	9.50 ± 0.5	AZ
46.2	3.592505	−30.401500	...			AZ
46.3	3.577519	−30.408700	...			AZ
53.1	3.579838	−30.401592	...	$4.26^{+0.97}_{-0.65}$...	DL
53.2	3.583548	−30.396700	DL
54.1	3.592350	−30.409892	...	$4.41^{+0.45}_{-0.35}$...	DL
54.2	3.588254	−30.410325	DL
54.5	3.600920	−30.400825	DL
55.1	3.597042	−30.404753	...	$1.58^{+0.06}_{-0.05}$...	DL
55.2	3.596417	−30.406125	DL
55.3	3.585744	−30.410100	DL
56.1	3.582542	−30.402272	...	$1.87^{+0.07}_{-0.07}$...	DL
56.2	3.586250	−30.400850	DL
56.3	3.584500	−30.399286	DL
56.4	3.596750	−30.396300	DL
59.1	3.584284	−30.408925	...	$2.37^{+0.13}_{-0.12}$...	MI
59.2	3.598125	−30.400981	MI
60.1	3.598075	−30.403989	...	$1.52^{+0.05}_{-0.05}$	1.70 ± 0.5	DL
60.2	3.595729	−30.407558	...			DL
60.3	3.587384	−30.410158	...			DL
62.1	3.577236	−30.395954	...	$5.43^{+0.42}_{-0.41}$	4.70 ± 0.5	...
62.2	3.587131	−30.388782

^a JM = Merten et al. (2011), HA14 = Atek et al. (2014), JR = Richard et al. (2014), AZ = Zitrin et al. (2014), DL = Lam et al. (2014), TJ = Johnson et al. (2014), MI = Ishigaki et al. (2015), MJ = Jauzac et al. (2015a), XW = Wang et al. (2015).

Table A2
MACS J0416.1–2403 Multiple Image Systems

ID	R.A.	Decl.	z_{spec}	z_{model}	Photo-z prior	Reference ^a
1.1	64.040797	−24.061616	1.896	AZ, LC
1.2	64.043472	−24.063514		AZ
1.3	64.047367	−24.068673		AZ
2.1	64.041168	−24.061851	1.893	AZ, CG
2.2	64.043021	−24.063010		AZ
2.3	64.047484	−24.068851		AZ
3.1	64.030772	−24.067118	1.989	AZ, CG
3.2	64.035254	−24.070993		AZ
3.3	64.041797	−24.075743		AZ
4.1	64.030782	−24.067218	1.989	AZ, CG
4.2	64.035181	−24.071001		AZ
4.3	64.041834	−24.075826		AZ
5.2	64.032637	−24.068647	2.095	AZ, AH
5.3	64.033531	−24.069452		AZ
5.4	64.043554	−24.076957		AZ
6.1	64.040013	−24.061830	...	$6.63^{+0.44}_{-0.37}$	6.30 ± 0.5	AZ
6.2	64.041600	−24.062680	...			AZ
6.3	64.049342	−24.072247
7.1	64.039808	−24.063085	2.086	AZ, CG
7.2	64.040652	−24.063578		AZ
7.3	64.047101	−24.071103		AZ
8.1	64.036602	−24.066122	...	$2.07^{+0.08}_{-0.07}$...	AZ
8.2	64.036837	−24.066332	AZ
8.3	64.046069	−24.075174
9.1	64.027032	−24.078564	...	$2.06^{+0.08}_{-0.08}$...	AZ
9.2	64.027521	−24.079095	AZ

Table A2 — *Continued*

ID	R.A.	Decl.	z_{spec}	z_{model}	Photo-z prior	Reference ^a
9.3	64.036450	-24.083976	MJ
10.1	64.026027	-24.077175	2.298	AZ, CG
10.2	64.028458	-24.079749	AZ
10.3	64.036698	-24.083885	AZ
11.1	64.039269	-24.070410	XX	AZ, SR
11.2	64.038302	-24.069735	AZ
11.3	64.034232	-24.066012	AZ
12.1	64.038256	-24.073685	...	$1.68^{+0.13}_{-0.10}$...	AZ
12.2	64.037690	-24.073301	AZ
13.1	64.027579	-24.072768	3.223	AZ, CG
13.2	64.032132	-24.075151	AZ
13.3	64.040336	-24.081532	AZ
14.1	64.026237	-24.074330	1.637	AZ, CG
14.2	64.031038	-24.078958	AZ
14.3	64.035826	-24.081317	AZ
15.1	64.026865	-24.075740	2.336	MJ, AH
15.2	64.029449	-24.078585	AZ
16.1	64.024075	-24.080905	1.964	AZ, AH
16.2	64.028342	-24.084548	AZ
16.3	64.031596	-24.085759	AZ
17.1	64.029814	-24.086351	2.218	AZ, CG
17.2	64.028609	-24.085968	AZ
17.3	64.023343	-24.081585	AZ
18.1	64.026096	-24.084238	...	$2.09^{+0.14}_{-0.12}$...	AZ
18.2	64.025061	-24.083325	AZ
23.1	64.044550	-24.072075	2.091	AZ, AH
23.2	64.039586	-24.066633	AZ
23.3	64.034321	-24.063719	AZ
25.1	64.044873	-24.061043	...	$2.60^{+0.11}_{-0.11}$...	AZ
25.2	64.045457	-24.061410	AZ
25.3	64.048241	-24.064501	MJ
25.4	64.049650	-24.066800	AZ
27.1	64.048153	-24.066957	2.107	MJ, AH
27.2	64.047480	-24.066017	MJ
27.3	64.042253	-24.060543	MJ
29.1	64.034270	-24.062989	2.285	MJ, AH
29.2	64.040469	-24.066330
29.3	64.044631	-24.071479	MJ
30.1	64.033043	-24.081763	...	$4.00^{+3.32}_{-1.30}$...	MJ
30.2	64.032671	-24.081576	MJ
31.1	64.023814	-24.077592	...	$1.80^{+0.06}_{-0.06}$	1.85 ± 0.5	MJ
31.2	64.030489	-24.082676	MJ
31.3	64.032415	-24.083751	MJ
33.1	64.028409	-24.083001	...	$5.69^{+0.33}_{-0.35}$	5.40 ± 0.5	MJ
33.2	64.035060	-24.085512	MJ
33.3	64.022992	-24.077267	MJ
34.1	64.029291	-24.073323	...	$5.75^{+0.42}_{-0.36}$	5.25 ± 0.5	MJ
34.2	64.030782	-24.074169	MJ
34.3	64.042074	-24.082294
35.1	64.037471	-24.083651	...	$3.58^{+0.19}_{-0.18}$	3.50 ± 0.5	MJ
35.2	64.029412	-24.079887	MJ
35.3	64.024950	-24.075019	MJ
37.1	64.033800	-24.082883	...	$2.91^{+0.15}_{-0.13}$...	MJ
37.2	64.031403	-24.081635	MJ
37.3	64.022888	-24.074327
38.1	64.033627	-24.083182	...	$3.06^{+0.16}_{-0.15}$	3.50 ± 0.5	MJ
38.2	64.031252	-24.081896	MJ
38.3	64.022698	-24.074590	MJ
40.1	64.037353	-24.063060	...	$2.47^{+0.09}_{-0.08}$...	MJ
40.2	64.040356	-24.064276	MJ
40.3	64.047109	-24.072435
41.1	64.037189	-24.063076	...	$2.48^{+0.09}_{-0.08}$...	MJ
41.2	64.040365	-24.064368	MJ
41.3	64.047064	-24.072493
42.1	64.046020	-24.070753	...	$2.55^{+0.10}_{-0.09}$...	MJ
42.2	64.042057	-24.065560	MJ
42.3	64.035772	-24.061944	MJ
43.1	64.035675	-24.082055	...	$3.05^{+0.33}_{-0.34}$	2.80 ± 0.5	MJ
43.2	64.031197	-24.079960	MJ
44.1	64.045266	-24.062760	...	$3.49^{+0.16}_{-0.14}$	3.30 ± 0.5	MJ
44.2	64.041552	-24.059996	MJ
44.3	64.049232	-24.068171	MJ

Table A2 — *Continued*

ID	R.A.	Decl.	z_{spec}	z_{model}	Photo-z prior	Reference ^a
46.1	64.038250	-24.080450	...	$2.18^{+0.07}_{-0.07}$...	MJ
46.2	64.026399	-24.072241	MJ
46.3	64.033072	-24.076201	MJ
47.1	64.026334	-24.076699	...	$3.58^{+0.36}_{-0.32}$	3.15 ± 0.5	MJ
47.2	64.028336	-24.079001	MJ
48.1	64.035452	-24.084679	...	$4.31^{+0.25}_{-0.25}$	4.30 ± 0.5	MJ
48.2	64.029248	-24.081793	MJ
48.3	64.023385	-24.076135	MJ
49.1	64.033945	-24.074570	...	$3.71^{+0.36}_{-0.35}$	3.80 ± 0.5	MJ
49.2	64.040168	-24.079871	MJ
50.1	64.034793	-24.074581	...	$2.77^{+0.12}_{-0.11}$...	MJ
50.2	64.039689	-24.078864	MJ
50.3	64.026788	-24.069208
51.1	64.040124	-24.080303	...	$3.66^{+0.20}_{-0.19}$	4.00 ± 0.5	MJ
51.2	64.033678	-24.074780	MJ
51.3	64.026638	-24.070476	MJ
52.1	64.045834	-24.065825	...	$4.20^{+0.37}_{-0.30}$...	MJ
52.2	64.047707	-24.068677	MJ
52.3	64.037706	-24.059832	MJ
53.1	64.046027	-24.068803	...	$2.96^{+0.14}_{-0.13}$	2.90 ± 0.5	MJ
53.2	64.044764	-24.066685	MJ
53.3	64.036196	-24.060650	MJ
54.1	64.046792	-24.071339	...	$2.34^{+0.08}_{-0.08}$...	MJ
54.2	64.041356	-24.064504	MJ
54.3	64.037185	-24.062435	MJ
55.1	64.035226	-24.064730	...	$3.32^{+0.19}_{-0.17}$...	MJ
55.2	64.046837	-24.075387
56.1	64.035673	-24.083593	...	$3.24^{+0.18}_{-0.16}$...	MJ
56.2	64.030097	-24.080918	MJ
56.3	64.023854	-24.075001	MJ
57.1	64.026221	-24.076024	...	$3.15^{+0.37}_{-0.32}$	3.15 ± 0.5	MJ
57.2	64.028847	-24.079126	MJ
59.1	64.035862	-24.072805	...	$1.92^{+0.05}_{-0.05}$...	MJ
59.2	64.039932	-24.075610	MJ
59.3	64.029096	-24.067650	MJ
60.1	64.026732	-24.073705	...	$3.78^{+0.30}_{-0.24}$...	MJ
60.2	64.039717	-24.082510	MJ
61.1	64.026737	-24.073536	...	$3.73^{+0.26}_{-0.22}$...	MJ
61.2	64.039762	-24.082376	MJ
63.1	64.025548	-24.076658	...	$4.10^{+0.27}_{-0.24}$	3.90 ± 0.5	MJ
63.2	64.028146	-24.079641	MJ
63.3	64.037916	-24.084480	MJ
65.1	64.042583	-24.075535	...	$5.25^{+0.52}_{-0.46}$...	MJ
65.2	64.028854	-24.064618	MJ
68.1	64.036092	-24.073358	...	$2.59^{+0.10}_{-0.09}$...	MJ
68.2	64.040362	-24.076479	MJ
68.3	64.028008	-24.067271	MJ
69.1	64.036267	-24.074226	...	$1.61^{+0.11}_{-0.09}$...	MJ
69.2	64.037663	-24.075272	MJ
72.1	64.031950	-24.071318	...	$3.03^{+0.57}_{-0.41}$...	MJ
72.2	64.030927	-24.070470	MJ
74.1	64.030730	-24.068882	...	$2.25^{+0.07}_{-0.07}$	2.40 ± 0.5	...
74.2	64.033526	-24.071381
74.3	64.042442	-24.077683
78.1	64.030380	-24.081610	...	$2.77^{+0.43}_{-0.37}$
78.2	64.034524	-24.083701
82.1	64.026265	-24.068699	...	$3.77^{+0.27}_{-0.20}$
82.2	64.040054	-24.079110
82.3	64.034916	-24.074576
83.1	64.030745	-24.070510	...	$4.06^{+0.89}_{-0.57}$
83.2	64.031722	-24.071343
84.1	64.040492	-24.075476	...	$2.00^{+0.10}_{-0.09}$...	JD
84.2	64.036063	-24.072404	JD
85.1	64.040438	-24.075768	...	$2.03^{+0.10}_{-0.09}$...	JD
85.2	64.035960	-24.072461	JD
86.1	64.045104	-24.072335	...	$3.81^{+0.49}_{-0.47}$...	JD
86.2	64.040084	-24.066734	JD
87.1	64.045363	-24.072537	...	$3.76^{+0.84}_{-0.49}$...	JD

Table A2 — *Continued*

ID	R.A.	Decl.	z_{spec}	z_{model}	Photo-z prior	Reference ^a
87.2	64.040000	-24.066651	JD
88.1	64.045503	-24.072676	...	$3.63^{+0.71}_{-0.49}$...	JD
88.2	64.039936	-24.066618	JD
89.1	64.037673	-24.061023	...	$4.24^{+0.32}_{-0.28}$
89.2	64.042884	-24.063891
89.3	64.048181	-24.070889
90.1	64.038892	-24.060636	...	$6.83^{+0.40}_{-0.41}$	6.40 ± 0.5	...
90.2	64.043317	-24.062964
90.3	64.049296	-24.071014
91.1	64.043575	-24.059000	...	$5.92^{+0.41}_{-0.41}$	6.10 ± 0.5	...
91.2	64.047846	-24.062067
91.3	64.050621	-24.065758
92.1	64.047138	-24.061139	...	$6.52^{+0.51}_{-0.39}$	5.90 ± 0.5	...
92.2	64.050867	-24.066530
93.1	64.038639	-24.083404	...	$6.84^{+0.97}_{-1.00}$
93.2	64.024434	-24.073911

^a LC = Christensen et al. (2012), AZ = Zitrin et al. (2013), MJ = Jauzac et al. (2014), CG = Grillo et al. (2015a), JD = Diego et al. (2015a), AH = Hoag et al. (in prep.), SR = Rodney et al. (in prep.).

Table A3
MACS J0717.5+3745 Multiple Image Systems

ID	R.A.	Decl.	z_{spec}	z_{model}	Photo-z prior	Reference ^a
1.1	109.395338	+37.741175	2.963	AZ, ML
1.2	109.393826	+37.740092		AZ
1.3	109.390988	+37.738286		AZ
1.4	109.384352	+37.736947		AZ
1.5	109.405784	+37.761374		EV
2.1	109.392813	+37.741003	...	$2.82^{+0.18}_{-0.11}$...	AZ
2.2	109.390434	+37.739247	AZ
3.1	109.398546	+37.741503	1.855	AZ, ML
3.2	109.394459	+37.739172		AZ
3.3	109.407155	+37.753830		ML
4.1	109.380870	+37.750119	1.855	AZ, KS
4.2	109.376438	+37.744689		AZ
4.3	109.391094	+37.763300		AZ
5.1	109.379908	+37.746861	...	$4.45^{+0.18}_{-0.19}$	5.10 ± 0.5	AZ
5.2	109.377917	+37.742803	...			AZ
5.3	109.400034	+37.767403	...			ML
6.1	109.364357	+37.757097	...	$2.04^{+0.04}_{-0.03}$...	AZ
6.2	109.362705	+37.752681	AZ
6.3	109.373863	+37.769703	AZ
7.1	109.366570	+37.766339	...	$2.07^{+0.04}_{-0.04}$...	AZ
7.2	109.365037	+37.764119	AZ
7.3	109.359047	+37.751781	AZ
8.1	109.366652	+37.769674	...	$2.61^{+0.07}_{-0.07}$...	AZ
8.2	109.362062	+37.763125	AZ
8.3	109.356509	+37.751928	AZ
12.1	109.385165	+37.751836	1.710	AZ, TT
12.2	109.377617	+37.742914		AZ
12.3	109.391219	+37.760630		AZ
13.1	109.385674	+37.750722	2.547	AZ, ML
13.2	109.377564	+37.739614		AZ
13.3	109.396212	+37.763333		AZ
14.1	109.388791	+37.752164	1.855	ML, ML
14.2	109.379664	+37.739703		ML
14.3	109.396192	+37.760419		ML
15.1	109.367663	+37.772058	2.405	ML, ML
15.2	109.358624	+37.760133		ML
15.3	109.356540	+37.754641		ML
16.1	109.369170	+37.773291	...	$3.03^{+0.06}_{-0.06}$...	ML
16.2	109.358561	+37.759558	ML
16.3	109.356930	+37.753699	ML
17.1	109.369371	+37.771866	...	$2.48^{+0.05}_{-0.05}$...	ML
17.2	109.359393	+37.758839	ML
17.3	109.358227	+37.753608	ML
17.4	109.360754	+37.758241	JD
18.1	109.364249	+37.768633	...	$2.04^{+0.06}_{-0.06}$...	ML
18.2	109.361215	+37.764333	ML

Table A3 — *Continued*

ID	R.A.	Decl.	z_{spec}	z_{model}	Photo-z prior	Reference ^a
19.1	109.409067	+37.754682	6.387	EV
19.2	109.407728	+37.742741	EV
19.3	109.381057	+37.731611	JR
20.1	109.374191	+37.765149	...	$2.58^{+0.24}_{-0.25}$...	JD
20.2	109.373400	+37.764658	JD
23.1	109.379564	+37.762852	...	$3.84^{+0.40}_{-0.35}$	3.50 ± 0.5	JD
23.2	109.378995	+37.762003	JD
25.1	109.380288	+37.744750	...	$4.53^{+0.18}_{-0.23}$	5.00 ± 0.5	JD
25.2	109.379513	+37.742756	JD
25.3	109.402914	+37.766408	JD
25.4	109.386063	+37.742033
27.1	109.397351	+37.747949	...	$2.25^{+0.64}_{-0.75}$...	JD
27.2	109.397551	+37.747566	JD
29.1	109.400879	+37.743175	...	$1.61^{+0.02}_{-0.02}$...	JD
29.2	109.392875	+37.738603	JD
29.3	109.406088	+37.749953	JD
31.1	109.374705	+37.756359	...	$1.55^{+0.02}_{-0.02}$...	JD
31.2	109.371020	+37.750555	JD
31.3	109.381612	+37.764983	JD
32.1	109.369513	+37.757724	...	$2.43^{+0.04}_{-0.05}$	3.00 ± 0.5	JD
32.2	109.380947	+37.769383	JD
32.3	109.366249	+37.749216	JD
33.1	109.383753	+37.758266	...	$3.87^{+0.08}_{-0.10}$...	JD
33.2	109.386605	+37.764129	JD
33.3	109.370353	+37.738692	JD
36.1	109.364321	+37.771974	...	$2.59^{+0.08}_{-0.07}$...	JD
36.2	109.358243	+37.763341	JD
36.3	109.353315	+37.755850	JD
45.1	109.389817	+37.739200	...	$3.06^{+0.25}_{-0.20}$...	JD
45.2	109.383456	+37.737881	JD
49.1	109.402967	+37.733258	...	$4.00^{+0.36}_{-0.36}$...	JD
49.2	109.392978	+37.730708	JD
50.1	109.374442	+37.743736	...	$2.97^{+0.08}_{-0.07}$...	JD
50.2	109.379582	+37.750708	JD
50.3	109.392803	+37.767181	JD
52.2	109.360222	+37.760497	...	$3.02^{+0.27}_{-0.18}$...	JD
52.3	109.357034	+37.752486	JD
53.1	109.370197	+37.761283	...	$2.55^{+0.06}_{-0.07}$...	JD
53.2	109.379324	+37.768266	JD
53.3	109.365095	+37.747151	JD
55.1	109.405801	+37.731841	...	$4.79^{+0.26}_{-0.24}$	4.60 ± 0.5	JD
55.2	109.397047	+37.729001	JD
55.3	109.414033	+37.741602
56.1	109.393140	+37.762794	...	$3.92^{+0.13}_{-0.14}$...	JD
56.2	109.387349	+37.755964	JD
56.3	109.375753	+37.735622	JD
57.1	109.392990	+37.762203	...	$3.91^{+0.12}_{-0.12}$...	JD
57.2	109.388044	+37.756514	JD
57.3	109.375941	+37.735131	JD
58.1	109.393003	+37.762389	...	$4.01^{+0.10}_{-0.10}$...	JD
58.2	109.387824	+37.756392	JD
58.3	109.375824	+37.735178	JD
60.1	109.402547	+37.763613	...	$2.85^{+0.06}_{-0.07}$	3.00 ± 0.5	JD
60.2	109.381086	+37.740666	JD
60.3	109.380654	+37.741346	JD
60.4	109.387206	+37.741291	JD
60.5	109.382704	+37.744707	JD
61.1	109.392209	+37.760494	...	$2.67^{+0.13}_{-0.13}$	3.15 ± 0.5	JD
61.2	109.389374	+37.757278	JD
62.1	109.379533	+37.745114	...	$3.85^{+0.44}_{-0.38}$	3.60 ± 0.5	JD
62.2	109.379020	+37.744105	JD
63.1	109.372561	+37.749536	...	$2.93^{+0.21}_{-0.19}$	3.40 ± 0.5	JD
63.2	109.373289	+37.751282	JD
64.1	109.387693	+37.738889	...	$3.79^{+0.15}_{-0.10}$	3.85 ± 0.5	JD
64.2	109.383957	+37.738396	JD
64.3	109.405246	+37.763783
64.4	109.383980	+37.743955
65.1	109.388637	+37.739259	...	$4.40^{+0.14}_{-0.26}$	4.10 ± 0.5	JD
65.2	109.382017	+37.738436	JD

Table A3 — *Continued*

ID	R.A.	Decl.	z_{spec}	z_{model}	Photo-z prior	Reference ^a
65.3	109.383471	+37.744588
65.4	109.404961	+37.764683
66.1	109.386218	+37.751924	...	$5.78^{+0.26}_{-0.21}$	6.20 ± 0.5	...
66.2	109.376999	+37.736450
66.3	109.399102	+37.764959
67.1	109.385440	+37.758508	...	$4.19^{+0.14}_{-0.12}$	4.50 ± 0.5	...
67.2	109.387777	+37.762834
67.3	109.371791	+37.737295
68.1	109.383107	+37.762585	...	$4.04^{+0.27}_{-0.26}$	4.00 ± 0.5	...
68.2	109.382235	+37.760399
69.1	109.390481	+37.737919	...	$3.13^{+0.11}_{-0.22}$
69.2	109.384688	+37.736875
70.1	109.365316	+37.747671	...	$3.40^{+0.12}_{-0.10}$	4.00 ± 0.5	...
70.2	109.368518	+37.758292
70.3	109.382338	+37.770699
71.1	109.362599	+37.747559	...	$3.26^{+0.10}_{-0.08}$
71.2	109.366909	+37.760808
71.3	109.378027	+37.770166
72.1	109.362867	+37.747774	...	$3.24^{+0.07}_{-0.08}$
72.2	109.366909	+37.760366
72.3	109.378480	+37.770341
73.1	109.362941	+37.747799	...	$3.26^{+0.07}_{-0.08}$
73.2	109.366888	+37.760233
73.3	109.378606	+37.770383
74.1	109.373152	+37.744011	...	$3.80^{+0.17}_{-0.15}$	4.50 ± 0.5	...
74.2	109.378399	+37.751095
74.3	109.392850	+37.768771
75.1	109.373027	+37.745508	...	$4.49^{+0.19}_{-0.22}$
75.2	109.377178	+37.750574
75.3	109.393355	+37.770141
76.1	109.370552	+37.745834	...	$3.60^{+0.11}_{-0.11}$	4.50 ± 0.5	...
76.2	109.376077	+37.753657
76.3	109.388875	+37.769833
77.1	109.363617	+37.750477	...	$3.43^{+0.17}_{-0.14}$
77.2	109.365372	+37.756216
77.3	109.380145	+37.772541
78.1	109.367431	+37.756481	...	$3.32^{+0.11}_{-0.11}$	4.00 ± 0.5	...
78.2	109.365128	+37.749532
78.3	109.382085	+37.771633
79.1	109.367048	+37.746459	...	$3.38^{+0.11}_{-0.10}$	4.10 ± 0.5	...
79.2	109.371065	+37.758450
79.3	109.384278	+37.770033
80.1	109.372394	+37.739899	...	$4.62^{+0.16}_{-0.15}$	5.10 ± 0.5	...
80.2	109.381475	+37.754354
80.3	109.391454	+37.767049
81.1	109.373064	+37.739655	...	$3.87^{+0.08}_{-0.10}$	4.00 ± 0.5	...
81.2	109.382140	+37.754277
81.3	109.391518	+37.766093
82.1	109.373004	+37.739002	...	$4.53^{+0.22}_{-0.17}$	5.00 ± 0.5	...
82.2	109.382391	+37.754409
82.3	109.391816	+37.766214
83.1	109.402100	+37.731199	...	$2.49^{+0.10}_{-0.10}$	2.60 ± 0.5	...
83.2	109.404937	+37.732524
84.1	109.397229	+37.729200	...	$4.67^{+0.32}_{-0.36}$
84.2	109.404811	+37.731449
85.1	109.379628	+37.746559	...	$4.33^{+0.16}_{-0.20}$	4.50 ± 0.5	...
85.2	109.377965	+37.743293
85.3	109.399954	+37.767516

^a AZ = Zitrin et al. (2009), ML = Limousin et al. (2012), KS = Schmidt et al. (2014), EV = Vanzella et al. (2014), JR = Richard et al. (2014), JD = Diego et al. (2015b), TT = Treu et al. (2015b)

Table A4
MACS J1149.6+2223 Multiple Image Systems

ID	R.A.	Decl.	z_{spec}	z_{model}	Photo-z prior	Reference ^a
1.1	177.397003	+22.396003	1.488	AZ, GS
1.2	177.399420	+22.397442		AZ
1.3	177.403420	+22.402442		AZ

Table A4 — *Continued*

ID	R.A.	Decl.	z_{spec}	z_{model}	Photo-z prior	Reference ^a
2.1	177.402419	+22.389753	1.894	AZ, GS
2.2	177.406044	+22.392480	AZ
2.3	177.406586	+22.392889	AZ
3.1	177.390753	+22.399850	3.129	AZ, MJ, CG
3.2	177.392711	+22.403083	AZ
3.3	177.401295	+22.407191	AZ
4.1	177.393003	+22.396828	2.949	AZ, CG
4.2	177.394378	+22.400739	AZ
4.3	177.404170	+22.406130	AZ
5.1	177.399753	+22.393064	2.800	AZ, GB
5.2	177.401086	+22.393828	AZ
5.3	177.407920	+22.403555	AZ
6.1	177.399711	+22.392547	...	$2.79^{+0.07}_{-0.06}$...	AZ
6.2	177.401836	+22.393861	AZ
6.3	177.408045	+22.402508	AZ
7.1	177.398961	+22.391342	...	$2.67^{+0.08}_{-0.08}$...	AZ
7.2	177.403420	+22.394272	AZ
7.3	177.407586	+22.401244	AZ
8.1	177.398503	+22.394353	...	$2.84^{+0.08}_{-0.08}$...	AZ
8.2	177.399794	+22.395047	AZ
8.4	177.407092	+22.404722	WZ
13.1	177.403711	+22.397789	1.240	WZ, GB
13.2	177.402836	+22.396658	WZ
13.3	177.400045	+22.393861	WZ
14.1	177.391667	+22.403506	3.703	JR, GB, CG
14.2	177.390842	+22.402639	JR
21.1	177.404496	+22.386697	...	$3.04^{+0.12}_{-0.12}$...	MJ
21.2	177.407986	+22.389053	MJ
21.3	177.409082	+22.390411	MJ
23.1	177.393012	+22.411422	...	$1.26^{+1.27}_{-0.52}$...	TT
23.2	177.393083	+22.411458	TT
23.3	177.393154	+22.411475	TT
24.1	177.392853	+22.412872	...	$2.05^{+0.44}_{-0.45}$	3.50 ± 0.5	GS
24.2	177.393541	+22.413069	GS
24.3	177.395042	+22.412697	GS
25.1	177.404283	+22.398775	...	$3.18^{+2.25}_{-1.58}$...	TT
25.2	177.404117	+22.398603	TT
26.1	177.410345	+22.388753	...	$3.72^{+0.20}_{-0.18}$	3.30 ± 0.5	MJ
26.2	177.409211	+22.387689	MJ
26.3	177.406245	+22.385372	MJ
28.1	177.395296	+22.391825	...	$3.03^{+0.13}_{-0.11}$	3.15 ± 0.5	MJ
28.2	177.402154	+22.396747	MJ
28.3	177.405621	+22.402436	MJ
29.1	177.400146	+22.390156	3.214	MJ, CG
29.2	177.404037	+22.392889	MJ
29.3	177.409067	+22.400242	MJ
30.1	177.400483	+22.395444	...	$2.92^{+0.11}_{-0.11}$...	TT
30.2	177.406829	+22.404517	TT
31.1	177.407646	+22.396789	...	$1.75^{+0.03}_{-0.03}$...	TT
31.2	177.402242	+22.391489	TT
31.3	177.403533	+22.392586	TT
32.1	177.409945	+22.387244	...	$5.03^{+0.22}_{-0.22}$	4.80 ± 0.5	MJ
32.2	177.406570	+22.384511	MJ
32.3	177.411228	+22.388461	MJ
33.1	177.409607	+22.386661	...	$6.66^{+0.28}_{-0.30}$	6.50 ± 0.5	MJ
33.2	177.406678	+22.384322	MJ
33.3	177.412078	+22.389056	MJ
34.1	177.405196	+22.386042	...	$3.62^{+0.15}_{-0.14}$...	MJ
34.2	177.408208	+22.388119	MJ
34.3	177.410374	+22.390625	MJ
35.1	177.407636	+22.385647	...	$3.82^{+0.18}_{-0.25}$...	TT
35.2	177.408632	+22.386453	TT
35.3	177.411328	+22.388997	TT
36.1	177.404421	+22.397303	...	$1.34^{+0.05}_{-0.04}$...	TT
36.2	177.403971	+22.396039	TT
37.1	177.404533	+22.395761	...	$1.37^{+0.04}_{-0.04}$...	TT
37.2	177.404937	+22.396397	TT
38.1	177.400725	+22.392411	...	$8.39^{+0.46}_{-0.54}$	8.40 ± 0.5	...
38.2	177.400567	+22.392317
39.1	177.412204	+22.394883	...	$5.63^{+0.34}_{-0.34}$	6.50 ± 0.5	...
39.2	177.404455	+22.386872

Table A4 — *Continued*

ID	R.A.	Decl.	z_{spec}	z_{model}	Photo-z prior	Reference ^a
40.1	177.390938	+22.399858	...	$3.15^{+0.09}_{-0.09}$
40.2	177.392417	+22.402561
40.3	177.401642	+22.407169
<i>SN Refsdal</i>						
S1	177.398225	+22.395628	1.488	PK, GS
S2	177.397713	+22.395781	PK
S3	177.397371	+22.395531	PK
S4	177.397800	+22.395181	PK
<i>Knot in System 1</i>						
1.2.1	177.396615	+22.396308	1.488	GS, GS
1.2.2	177.398978	+22.397892	GS
1.2.3	177.403041	+22.402689	GS
1.2.4	177.397765	+22.398780	GS
1.2.6	177.398674	+22.398225	SR
1.13.1	177.396974	+22.396636	1.488	GS, GS
1.13.2	177.398832	+22.397717	GS
1.13.3	177.403311	+22.402814	GS
1.13.4	177.397907	+22.398433	GS
1.16.1	177.397446	+22.396394	1.488	GS
1.16.2	177.399154	+22.397219	GS
1.16.3	177.403596	+22.402647	GS
1.17.1	177.398140	+22.396353	1.488	GS, GS
1.17.2	177.399274	+22.396839	GS
1.17.3	177.403845	+22.402569	GS
1.19.1	177.396892	+22.395761	1.488	SR
1.19.2	177.399538	+22.397483	SR
1.19.3	177.403367	+22.402286	SR
1.19.5	177.399962	+22.397094	SR
1.23.1	177.396724	+22.395372	1.488	GS, GS
1.23.2	177.399757	+22.397494	GS
1.23.3	177.403257	+22.402025	GS
1.23.5	177.400133	+22.397203	SR
1.30.1	177.398171	+22.395469	1.488	SR, GS
1.30.2	177.398008	+22.395231	SR
1.30.3	177.397308	+22.395372	SR
1.30.4	177.397896	+22.395728	SR

^a AZ = Zitrin & Broadhurst (2009), GS = Smith et al. (2009), WZ = Zheng et al. (2012), SR = Rau et al. (2014), JR = Richard et al. (2014), PK = Kelly et al. (2015b), MJ = Jauzac et al. (2015b), TT = Treu et al. (2015a), CG = Grillo et al. (2015b), GB = Brammer et al. (in prep.).

* We note that in the identification of the multiple images, we do not refer to Jauzac et al. (2015b), which was posted to arXiv very recently. All of the multiple images labeled Jauzac et al. (2015b) in this table are also presented in Treu et al. (2015a).

B. LISTS OF DROPOUT GALAXY CANDIDATES

The list of dropout galaxy candidates is given in Tables B1–B3.

Table B1
Dropout galaxy candidates at $z \sim 6 - 7$ in the four HFF cluster fields.

ID ^a	ID ^{a,b}	R.A.	Decl.	$i_{814} - Y_{105}$	$Y_{105} - J_{125}$	J_{125}^b	μ_{best}	μ^c	z_{photo}	Reference ^d
HFF1C										
2251-4556	i1	3.593804	-30.415447	2.68 ± 0.31	0.05 ± 0.05	26.10 ± 0.03	3.64	$3.93^{+0.40}_{-0.33}$	$6.6^{+0.8}_{-0.7}$	A14, I, A15
1695-4527	i2	3.570654	-30.414659	1.33 ± 0.10	0.11 ± 0.05	26.22 ± 0.04	1.47	$1.54^{+0.09}_{-0.06}$	$6.0^{+0.7}_{-0.7}$	A14, I, A15
2549-3119	i3	3.606222	-30.386644	1.07 ± 0.08	0.08 ± 0.05	26.26 ± 0.04	1.55	$1.65^{+0.08}_{-0.06}$	$5.8^{+0.7}_{-0.6}$	A14, I, A15
1930-4181	i4	3.580453	-30.405043	> 2.36	0.17 ± 0.09	26.61 ± 0.06	4.47	$4.90^{+0.43}_{-0.36}$	$6.8^{+0.8}_{-0.7}$	A14, I, A15
2516-4570	i5	3.604865	-30.415839	0.92 ± 0.13	0.06 ± 0.07	26.67 ± 0.06	2.84	$3.02^{+0.24}_{-0.22}$	$5.6^{+0.7}_{-0.6}$...
2348-3454	i6	3.597834	-30.395961	> 2.13	0.27 ± 0.10	26.79 ± 0.07	3.31	$3.47^{+0.27}_{-0.21}$	$7.0^{+0.8}_{-0.8}$	I, A15
2178-2458	i7	3.590761	-30.379409	0.96 ± 0.13	-0.16 ± 0.09	27.07 ± 0.08	1.68	$1.78^{+0.12}_{-0.09}$	$5.9^{+0.6}_{-0.7}$	I
2047-3526	i8	3.585322	-30.397958	> 1.83	0.13 ± 0.14	27.19 ± 0.11	3.23	$3.76^{+0.36}_{-0.34}$	$6.8^{+0.7}_{-0.8}$	WZ14, I, A15
2425-4143	i9	3.601072	-30.403991	1.11 ± 0.22	0.00 ± 0.12	27.27 ± 0.09	3.74	$3.89^{+0.32}_{-0.22}$	$6.0^{+0.6}_{-0.7}$	A14, I, A15
2414-4370	i10	3.600619	-30.410296	> 1.97	-0.06 ± 0.12	27.29 ± 0.10	11.88	$12.74^{+2.00}_{-1.80}$	$6.4^{+0.7}_{-0.7}$	I, A15
2482-2595	i11	3.603426	-30.383219	0.87 ± 0.14	-0.13 ± 0.11	27.30 ± 0.09	1.48	$1.57^{+0.08}_{-0.07}$	$5.8^{+0.7}_{-0.7}$	I, A15, C
2477-4372	i12	3.603214	-30.410351	> 1.89	-0.03 ± 0.13	27.34 ± 0.10	4.02	$4.17^{+0.34}_{-0.26}$	$6.3^{+0.7}_{-0.7}$	A14, WZ14, I, A15
2230-4479	i13	3.592944	-30.413328	1.44 ± 0.29	-0.09 ± 0.14	27.36 ± 0.11	6.81	$7.45^{+0.89}_{-0.75}$	$6.1^{+0.7}_{-0.7}$	I, A15
1845-3107	i14	3.576889	-30.386328	> 1.45	0.13 ± 0.18	27.46 ± 0.13	8.00	$7.99^{+1.98}_{-1.19}$	$6.1^{+0.8}_{-0.7}$	I, A15
2040-4471	i15	3.585016	-30.413084	0.86 ± 0.16	-0.24 ± 0.14	27.46 ± 0.12	2.95	$3.10^{+0.24}_{-0.19}$	$5.7^{+0.6}_{-1.1}$	I

Table B1 — *Continued*

ID ^a	ID ^{a,b}	R.A.	Decl.	$i_{814} - Y_{105}$	$Y_{105} - J_{125}$	J_{125}^b	μ_{best}	μ^c	z_{photo}	Reference ^d
1911-4242	i16	3.579635	-30.406723	1.06 ± 0.33	0.08 ± 0.19	27.53 ± 0.15	3.45	$3.75^{+0.31}_{-0.25}$	$5.6^{+0.7}_{-5.3}$...
2616-3070	i17	3.609003	-30.385283	1.35 ± 0.26	-0.07 ± 0.14	27.57 ± 0.12	1.44	$1.52^{+0.07}_{-0.05}$	$6.1^{+0.7}_{-0.7}$	I, A ₁₅
2509-4337	i18	3.604563	-30.409364	1.43 ± 0.45	0.12 ± 0.18	27.63 ± 0.13	3.12	$3.21^{+0.25}_{-0.16}$	$6.1^{+0.7}_{-0.8}$	I, A ₁₅
2274-2562	i19	3.594752	-30.382305	0.84 ± 0.21	-0.17 ± 0.17	27.73 ± 0.14	1.85	$1.99^{+0.13}_{-0.11}$	$0.1^{+3.8}_{-0.1}$...
2364-4454	i20	3.598515	-30.412612	> 1.18	0.16 ± 0.25	27.94 ± 0.18	15.56	$17.67^{+6.16}_{-4.03}$	$6.6^{+0.7}_{-5.3}$...
1991-3429	i21	3.582960	-30.395261	> 0.90	0.14 ± 0.26	27.97 ± 0.19	9.25	$9.90^{+0.93}_{-0.91}$	$1.3^{+5.2}_{-1.1}$...
2172-2471	i22	3.590518	-30.379763	> 1.36	-0.02 ± 0.24	28.10 ± 0.19	1.73	$1.84^{+0.13}_{-0.09}$	$6.1^{+0.7}_{-1.5}$	I, A ₁₅
HFF2C										
0949-5187	i1	64.039545	-24.088540	1.08 ± 0.10	-0.01 ± 0.05	26.37 ± 0.04	1.54	$1.54^{+0.05}_{-0.04}$	$5.9^{+0.7}_{-0.7}$	B
1148-3434	i2	64.047846	-24.062066	1.63 ± 0.12	-0.16 ± 0.06	26.64 ± 0.05	19.12	$18.64^{+2.94}_{-2.36}$	$6.2^{+0.7}_{-0.7}$	B, C
1131-3400	i3	64.047138	-24.061138	0.98 ± 0.10	-0.05 ± 0.08	26.92 ± 0.06	11.18	$10.76^{+1.05}_{-0.92}$	$5.9^{+0.6}_{-0.7}$...
0899-3404	i4	64.037485	-24.061238	1.26 ± 0.20	-0.01 ± 0.11	27.05 ± 0.09	3.38	$3.29^{+0.19}_{-0.19}$	$6.0^{+0.7}_{-0.6}$	C
0960-3425	i5	64.040012	-24.061829	1.74 ± 0.36	0.00 ± 0.14	27.32 ± 0.11	11.10	$10.25^{+1.02}_{-0.88}$	$6.3^{+0.7}_{-0.7}$	B, C
1147-4580	i6	64.047818	-24.082800	> 1.85	0.23 ± 0.13	27.38 ± 0.09	1.40	$1.40^{+0.04}_{-0.04}$	$6.8^{+0.7}_{-0.8}$	C
1220-3595	i7	64.050865	-24.066531	1.04 ± 0.18	-0.07 ± 0.11	27.38 ± 0.09	3.55	$3.46^{+0.17}_{-0.18}$	$5.9^{+0.7}_{-0.7}$	C
1156-3446	i8	64.048176	-24.062404	1.55 ± 0.22	-0.18 ± 0.12	27.41 ± 0.10	31.58	$31.46^{+9.62}_{-6.09}$	$6.2^{+0.7}_{-0.7}$...
0768-5032	i9	64.032020	-24.084227	0.82 ± 0.24	-0.01 ± 0.19	27.47 ± 0.15	6.32	$6.62^{+0.83}_{-0.68}$	$5.5^{+0.6}_{-4.8}$...
1181-3480	i10	64.049226	-24.063349	1.77 ± 0.26	-0.22 ± 0.12	27.47 ± 0.10	68.19	$76.09^{+55.16}_{-21.58}$	$6.3^{+0.7}_{-0.7}$...
1030-3258	i11	64.042942	-24.057182	0.87 ± 0.20	-0.16 ± 0.16	27.52 ± 0.13	2.87	$2.82^{+0.13}_{-0.12}$	$5.7^{+0.6}_{-0.7}$...
0743-3348	i12	64.030960	-24.059683	> 1.49	0.32 ± 0.15	27.52 ± 0.11	1.80	$1.77^{+0.06}_{-0.06}$	$6.3^{+1.2}_{-5.5}$...
0778-3204	i13	64.032450	-24.055671	1.14 ± 0.28	0.03 ± 0.14	27.53 ± 0.11	1.74	$1.72^{+0.06}_{-0.06}$	$6.0^{+0.7}_{-0.7}$...
1105-5392	i14	64.046063	-24.094241	> 1.71	0.03 ± 0.14	27.53 ± 0.11	1.23	$1.23^{+0.02}_{-0.02}$	$6.5^{+0.7}_{-0.7}$...
0829-5229	i15	64.034556	-24.089700	1.22 ± 0.29	-0.03 ± 0.19	27.54 ± 0.15	1.78	$1.79^{+0.06}_{-0.06}$	$6.0^{+0.7}_{-0.9}$	C
1045-3324	i16	64.043574	-24.059000	1.36 ± 0.29	-0.19 ± 0.16	27.59 ± 0.14	5.20	$5.06^{+0.29}_{-0.26}$	$6.1^{+0.7}_{-0.7}$...
0856-4435	i17	64.035702	-24.078765	1.07 ± 0.37	0.16 ± 0.23	27.59 ± 0.16	16.04	$15.18^{+2.76}_{-2.03}$	$5.5^{+1.0}_{-5.2}$...
0933-3382	i18	64.038890	-24.060637	> 1.68	0.00 ± 0.18	27.66 ± 0.15	4.02	$3.90^{+0.22}_{-0.23}$	$6.4^{+0.8}_{-0.7}$...
1330-3565	i19	64.055426	-24.065698	0.90 ± 0.24	0.00 ± 0.16	27.77 ± 0.13	2.24	$2.19^{+0.09}_{-0.08}$	$5.7^{+0.7}_{-1.4}$...
1225-3594	i20	64.051077	-24.066511	1.29 ± 0.32	0.02 ± 0.16	27.78 ± 0.13	3.46	$3.36^{+0.17}_{-0.17}$	$6.0^{+0.8}_{-0.8}$	C
1308-3431	i21	64.054524	-24.061998	0.96 ± 0.20	-0.28 ± 0.18	27.89 ± 0.15	3.80	$3.71^{+0.16}_{-0.16}$	$5.7^{+0.7}_{-0.7}$...
0771-3205	i22	64.032155	-24.055706	1.03 ± 0.28	-0.31 ± 0.19	27.99 ± 0.16	1.77	$1.75^{+0.06}_{-0.06}$	$5.8^{+0.7}_{-1.1}$...
0924-5133	i23	64.038512	-24.087044	> 1.47	-0.36 ± 0.21	28.16 ± 0.18	1.71	$1.72^{+0.07}_{-0.06}$	$6.2^{+0.7}_{-1.1}$...
HFF3C										
3377-4319	i1	109.390738	+37.742218	1.09 ± 0.08	-0.07 ± 0.04	25.82 ± 0.04	60.69	$65.95^{+13.27}_{-9.90}$	$5.9^{+0.7}_{-0.7}$	B
3817-5168	i2	109.409066	+37.754682	1.52 ± 0.10	-0.05 ± 0.04	25.96 ± 0.04	4.96	$4.96^{+0.36}_{-0.28}$	$6.1^{+0.7}_{-0.7}$	B
3785-4338	i3	109.407728	+37.742741	1.48 ± 0.11	-0.07 ± 0.05	26.06 ± 0.04	8.40	$8.41^{+0.99}_{-1.16}$	$6.1^{+0.7}_{-0.7}$	B
3578-5538	i4	109.399102	+37.764959	1.57 ± 0.19	-0.00 ± 0.07	26.52 ± 0.06	6.59	$6.57^{+0.43}_{-0.50}$	$6.1^{+0.7}_{-0.7}$	B
3269-5069	i5	109.386219	+37.751924	1.73 ± 0.29	0.10 ± 0.09	26.66 ± 0.07	3.06	$3.07^{+0.19}_{-0.19}$	$6.3^{+0.7}_{-0.7}$	B
3342-3294	i6	109.389277	+37.724858	1.31 ± 0.24	0.12 ± 0.09	26.84 ± 0.07	2.35	$2.38^{+0.10}_{-0.08}$	$6.0^{+0.7}_{-0.6}$...
3145-3537	i7	109.381053	+37.731611	1.43 ± 0.23	-0.05 ± 0.09	26.87 ± 0.07	3.34	$3.37^{+0.20}_{-0.23}$	$6.1^{+0.7}_{-0.7}$...
3047-4112	i8	109.376996	+37.736450	1.31 ± 0.20	0.08 ± 0.09	26.96 ± 0.08	4.08	$4.10^{+0.22}_{-0.34}$	$6.0^{+0.7}_{-0.6}$...
3389-4210	i9	109.391220	+37.739172	1.17 ± 0.41	0.22 ± 0.20	27.38 ± 0.15	23.83	$23.16^{+4.89}_{-6.79}$	$5.9^{+0.7}_{-0.7}$...
3096-5100	i10	109.379016	+37.752792	1.04 ± 0.21	-0.17 ± 0.16	27.41 ± 0.14	4.81	$5.13^{+0.32}_{-0.26}$	$5.8^{+0.6}_{-0.7}$...
3318-5132	i11	109.388269	+37.753667	0.82 ± 0.26	0.04 ± 0.17	27.42 ± 0.13	5.43	$5.67^{+0.36}_{-0.50}$	$5.6^{+0.7}_{-1.2}$...
4047-4196	i12	109.418650	+37.738793	1.19 ± 0.27	-0.15 ± 0.17	27.48 ± 0.14	8.18	$8.91^{+1.50}_{-1.59}$	$5.9^{+0.6}_{-0.7}$...
3810-4541	i13	109.408780	+37.748379	1.15 ± 0.29	-0.01 ± 0.18	27.53 ± 0.14	95.69	$53.56^{+86.11}_{-18.62}$	$5.8^{+0.7}_{-0.6}$...
3585-5491	i14	109.399393	+37.763654	1.17 ± 0.39	0.18 ± 0.19	27.55 ± 0.15	7.21	$6.96^{+0.51}_{-0.76}$	$5.7^{+0.7}_{-5.0}$...
3411-4573	i15	109.392135	+37.749271	0.97 ± 0.32	-0.02 ± 0.19	27.60 ± 0.16	8.49	$11.78^{+5.97}_{-3.27}$	$5.7^{+0.6}_{-5.0}$...
2777-4506	i16	109.365722	+37.747409	> 1.44	0.20 ± 0.22	27.64 ± 0.17	4.38	$4.61^{+0.26}_{-0.24}$	$6.1^{+0.7}_{-1.4}$...
3981-4481	i17	109.415897	+37.746722	> 1.67	-0.08 ± 0.20	27.70 ± 0.17	15.31	$12.77^{+2.16}_{-1.53}$	$6.5^{+0.7}_{-0.8}$...
3096-4181	i18	109.379034	+37.738386	1.27 ± 0.34	-0.01 ± 0.17	27.73 ± 0.14	5.99	$6.13^{+0.37}_{-0.48}$	$6.0^{+0.7}_{-4.6}$...
3509-5294	i19	109.396250	+37.758188	> 1.38	-0.12 ± 0.23	27.88 ± 0.19	9.14	$7.45^{+1.32}_{-0.80}$	$6.2^{+0.7}_{-0.9}$...
3091-4467	i20	109.378815	+37.746314	> 1.72	-0.43 ± 0.22	28.11 ± 0.20	9.94	$10.49^{+0.89}_{-1.07}$	$6.4^{+0.7}_{-0.7}$...
HFF4C										
4025-5027	i1	177.417749	+22.417435	> 3.48	0.57 ± 0.03	25.21 ± 0.02	1.57	$1.59^{+0.12}_{-0.12}$	$7.5^{+0.8}_{-0.8}$...
3888-4567	i2	177.412018	+22.415777	1.11 ± 0.05	0.12 ± 0.03	25.52 ± 0.02	1.94	$2.04^{+0.28}_{-0.24}$	$5.8^{+0.7}_{-0.6}$	B
3321-2566	i3	177.388388	+22.382390	1.67 ± 0.14	-0.07 ± 0.05	26.21 ± 0.04	1.74	$1.64^{+0.05}_{-0.05}$	$6.3^{+0.7}_{-0.7}$	B
3180-3434	i4	177.382540	+22.395401	0.86 ± 0.09	0.07 ± 0.06	26.30 ± 0.04	2.28	$2.15^{+0.12}_{-0.11}$	$5.7^{+0.7}_{-0.6}$	B

Table B1 — *Continued*

ID ^a	ID ^{a,b}	R.A.	Decl.	$i_{814} - Y_{105}$	$Y_{105} - J_{125}$	J_{125}^b	μ_{best}	μ^c	z_{photo}	Reference ^d
3672-4342	i5	177.403011	+22.409501	1.07 ± 0.10	-0.07 ± 0.06	26.49 ± 0.05	3.68	$4.10^{+1.17}_{-0.58}$	$6.0^{+0.6}_{-0.7}$	B
4042-4205	i6	177.418442	+22.405696	0.91 ± 0.09	-0.08 ± 0.06	26.58 ± 0.05	1.77	$1.76^{+0.08}_{-0.07}$	$5.9^{+0.6}_{-0.7}$...
3910-4491	i7	177.412935	+22.413642	2.26 ± 0.31	-0.19 ± 0.08	26.72 ± 0.07	1.87	$1.99^{+0.40}_{-0.23}$	$6.4^{+0.7}_{-0.7}$...
4042-4207	i8	177.418456	+22.405770	0.98 ± 0.11	-0.11 ± 0.07	26.78 ± 0.06	1.77	$1.75^{+0.08}_{-0.07}$	$5.9^{+0.7}_{-0.7}$...
4046-4231	i9	177.418619	+22.406430	1.06 ± 0.14	0.05 ± 0.08	26.81 ± 0.06	1.73	$1.72^{+0.08}_{-0.07}$	$5.9^{+0.7}_{-0.6}$...
3952-5014	i10	177.414690	+22.417060	> 2.16	0.07 ± 0.11	27.04 ± 0.09	1.71	$1.74^{+0.15}_{-0.15}$	$6.5^{+0.7}_{-0.8}$...
3906-4324	i11	177.412777	+22.409016	> 1.76	0.42 ± 0.12	27.09 ± 0.08	1.95	$2.01^{+0.25}_{-0.13}$	$7.3^{+0.8}_{-1.4}$...
4047-4228	i12	177.418636	+22.406343	1.11 ± 0.18	-0.05 ± 0.10	27.11 ± 0.08	1.73	$1.72^{+0.08}_{-0.07}$	$5.9^{+0.7}_{-0.7}$...
3705-4446	i13	177.404410	+22.412397	> 1.88	0.33 ± 0.12	27.14 ± 0.09	3.50	$4.18^{+4.87}_{-1.10}$	$7.1^{+0.8}_{-1.5}$...
3830-3120	i14	177.409606	+22.386668	1.77 ± 0.38	0.11 ± 0.12	27.20 ± 0.09	6.21	$5.76^{+0.85}_{-0.94}$	$6.3^{+0.7}_{-0.7}$...
3765-3173	i15	177.406897	+22.388148	0.98 ± 0.22	0.13 ± 0.12	27.21 ± 0.09	5.15	$4.73^{+1.07}_{-1.03}$	$1.1^{+5.0}_{-0.5}$...
3889-3206	i16	177.412079	+22.389059	> 1.97	0.02 ± 0.13	27.31 ± 0.10	8.54	$8.27^{+0.92}_{-0.73}$	$6.6^{+0.7}_{-0.7}$...
4026-3382	i17	177.417760	+22.393947	1.11 ± 0.22	-0.01 ± 0.13	27.35 ± 0.10	3.17	$2.99^{+0.12}_{-0.11}$	$5.9^{+0.7}_{-0.9}$...
3231-2579	i18	177.384647	+22.382754	1.23 ± 0.24	-0.23 ± 0.14	27.42 ± 0.12	1.68	$1.60^{+0.05}_{-0.05}$	$6.0^{+0.7}_{-0.7}$...
3191-4433	i19	177.382991	+22.412040	> 1.59	0.43 ± 0.17	27.43 ± 0.11	6.95	$8.20^{+15.15}_{-3.25}$	$7.2^{+0.8}_{-1.3}$...
3665-4526	i20	177.402725	+22.414615	0.84 ± 0.19	-0.08 ± 0.14	27.45 ± 0.11	5.10	$5.52^{+2.97}_{-1.66}$	$5.8^{+0.6}_{-0.7}$...
4076-4033	i21	177.419863	+22.400937	1.48 ± 0.40	0.26 ± 0.16	27.46 ± 0.11	2.08	$2.02^{+0.07}_{-0.06}$	$6.1^{+1.0}_{-0.8}$...
3760-3035	i22	177.406675	+22.384327	> 1.73	0.04 ± 0.16	27.53 ± 0.12	6.51	$5.69^{+0.79}_{-1.06}$	$6.6^{+0.7}_{-0.8}$...
3791-4415	i23	177.407983	+22.411538	1.54 ± 0.37	-0.02 ± 0.15	27.54 ± 0.12	2.36	$2.61^{+0.91}_{-0.36}$	$6.1^{+0.7}_{-0.7}$...
3894-3418	i24	177.412259	+22.394967	> 1.55	0.12 ± 0.17	27.56 ± 0.12	7.10	$6.57^{+0.44}_{-0.38}$	$6.6^{+0.7}_{-0.8}$...
3305-4210	i25	177.387710	+22.405836	0.89 ± 0.24	0.05 ± 0.16	27.62 ± 0.12	11.19	$11.38^{+3.41}_{-2.00}$	$5.8^{+0.7}_{-0.8}$...
3892-3416	i26	177.412203	+22.394890	> 1.40	0.09 ± 0.19	27.74 ± 0.14	7.27	$6.72^{+0.46}_{-0.39}$	$6.6^{+0.7}_{-1.0}$...
3736-5005	i27	177.405705	+22.416817	> 1.34	0.25 ± 0.20	27.76 ± 0.15	2.58	$2.62^{+0.31}_{-0.33}$	$6.6^{+0.8}_{-5.4}$...
3991-3123	i28	177.416321	+22.386751	1.12 ± 0.35	0.09 ± 0.21	27.85 ± 0.16	3.56	$3.38^{+0.16}_{-0.13}$	$5.8^{+1.2}_{-4.9}$...
3405-3155	i29	177.391898	+22.387646	1.20 ± 0.43	0.04 ± 0.20	27.87 ± 0.15	2.38	$2.19^{+0.10}_{-0.09}$	$0.7^{+5.9}_{-0.6}$...
3419-3006	i30	177.392475	+22.383511	0.82 ± 0.28	-0.18 ± 0.19	27.87 ± 0.15	1.93	$1.79^{+0.07}_{-0.07}$	$5.6^{+0.7}_{-1.4}$...
3595-4157	i31	177.399818	+22.404384	0.84 ± 0.35	0.09 ± 0.24	27.92 ± 0.18	578.83	$119.66^{+241.09}_{-53.58}$	$0.3^{+4.0}_{-0.2}$...
4082-3192	i32	177.420086	+22.388672	0.89 ± 0.23	-0.31 ± 0.20	27.93 ± 0.17	3.01	$2.85^{+0.10}_{-0.10}$	$5.6^{+0.7}_{-4.8}$...
3312-2565	i33	177.388012	+22.382380	> 1.45	-0.13 ± 0.23	27.93 ± 0.19	1.73	$1.64^{+0.05}_{-0.05}$	$6.2^{+0.8}_{-1.0}$...
3282-4046	i34	177.386778	+22.401298	0.85 ± 0.22	-0.45 ± 0.20	28.06 ± 0.18	5.22	$4.99^{+0.47}_{-0.40}$	$5.6^{+0.7}_{-0.6}$...
3829-4199	i35	177.409561	+22.405545	> 1.09	0.01 ± 0.26	28.17 ± 0.20	2.45	$2.42^{+0.13}_{-0.12}$	$6.3^{+0.8}_{-2.2}$...

^a For simplicity, the part that represents the cluster name is omitted. Examples of full IDs are HFF1C-2251-4556 and HFF1C-i1.^b Short ID used only in this paper for simplification and clarity.^c Total magnitude.^d Median value and 1σ error of the magnification factor from the MCMC posterior distribution.^e A₁₄ = Atek et al. (2014), B = Bradley et al. (2014), WZ₁₄ = Zheng et al. (2014), I = Ishigaki et al. (2015), A₁₅ = Atek et al. (2015a), C = Coe et al. (2015).**Table B2**
Dropout galaxy candidates at $z \sim 8$ in the four HFF cluster fields.

ID ^a	ID ^{a,b}	R.A.	Decl.	$Y_{105} - J_{125}$	$J_{125} - JH_{140}$	JH_{140}^c	μ_{best}	μ^d	z_{photo}	Reference ^e
HFF1C										
2508-2496	Y1	3.604518	-30.380467	1.17 ± 0.07	0.04 ± 0.04	25.92 ± 0.03	1.31	$1.38^{+0.07}_{-0.05}$	$8.0^{+0.9}_{-0.9}$	L ₁₄ , A ₁₄ , WZ ₁₄ , I, A ₁₅ , C
2481-2561	Y2	3.603378	-30.382255	1.27 ± 0.15	0.14 ± 0.08	26.64 ± 0.05	1.40	$1.48^{+0.08}_{-0.06}$	$8.2^{+0.9}_{-0.9}$	WZ ₁₄ , I, A ₁₅ , C
2306-3089	Y3	3.596091	-30.385833	1.30 ± 0.15	0.06 ± 0.08	26.68 ± 0.05	2.04	$2.20^{+0.15}_{-0.12}$	$8.2^{+0.9}_{-0.9}$	WZ ₁₄ , I, A ₁₅ , C
2555-2515	Y4	3.606461	-30.380996	1.12 ± 0.13	-0.18 ± 0.09	26.95 ± 0.06	1.33	$1.40^{+0.07}_{-0.05}$	$8.0^{+0.8}_{-0.9}$	WZ ₁₄ , I, A ₁₅ , C
2492-2561	Y5	3.603859	-30.382264	1.92 ± 0.32	0.16 ± 0.10	26.99 ± 0.07	1.40	$1.48^{+0.08}_{-0.06}$	$8.4^{+0.9}_{-0.9}$	WZ ₁₄ , I, A ₁₅ , C
2557-2513	Y6	3.606576	-30.380924	1.10 ± 0.22	0.22 ± 0.13	27.17 ± 0.08	1.32	$1.39^{+0.07}_{-0.05}$	$7.9^{+0.9}_{-0.9}$	WZ ₁₄ , I, A ₁₅
2135-2432	Y7	3.588980	-30.378668	1.13 ± 0.18	-0.19 ± 0.12	27.30 ± 0.09	1.69	$1.79^{+0.12}_{-0.09}$	$8.0^{+0.8}_{-0.9}$	WZ ₁₄ , I, A ₁₅ , C
2495-2562	Y8	3.603997	-30.382304	1.05 ± 0.28	0.13 ± 0.18	27.61 ± 0.11	1.40	$1.48^{+0.08}_{-0.06}$	$7.9^{+0.9}_{-0.9}$	WZ ₁₄ , I, C
2216-4356	Y9	3.592349	-30.409892	0.60 ± 0.25	-0.30 ± 0.23	28.01 ± 0.18	8.57	$9.03^{+0.76}_{-0.70}$	$7.3^{+0.8}_{-2.0}$	WZ ₁₄ , I, A ₁₅
2521-2532	Y10	3.605062	-30.381463	0.84 ± 0.29	-0.16 ± 0.23	28.07 ± 0.17	1.35	$1.42^{+0.07}_{-0.06}$	$7.7^{+0.8}_{-6.4}$	I, A ₁₅
HFF2C										
1151-4540	Y1	64.047984	-24.081670	1.92 ± 0.18	0.01 ± 0.06	26.50 ± 0.04	1.43	$1.43^{+0.04}_{-0.04}$	$8.4^{+0.9}_{-0.9}$	L ₁₅ , C, M
0939-5354	Y2	64.039165	-24.093183	2.19 ± 0.30	0.18 ± 0.07	26.61 ± 0.05	1.39	$1.39^{+0.03}_{-0.03}$	$8.5^{+0.9}_{-0.9}$	L ₁₅ , M
1153-4531	Y3	64.048057	-24.081431	2.28 ± 0.46	0.49 ± 0.10	26.80 ± 0.06	1.43	$1.44^{+0.04}_{-0.04}$	$8.7^{+0.9}_{-1.0}$	L ₁₅ , C

Table B2 — *Continued*

ID ^a	ID ^{a,b}	R.A.	Decl.	$Y_{105} - J_{125}$	$J_{125} - JH_{140}$	JH_{140} ^c	μ_{best}	μ^d	z_{photo}	Reference ^e
0901-5171	Y4	64.037567	-24.088109	1.94 ± 0.50	0.12 ± 0.17	27.56 ± 0.12	1.69	$1.70^{+0.06}_{-0.06}$	$8.4^{+0.9}_{-1.0}$	L ₁₅ , M
1447-3538	Y5	64.060329	-24.064958	0.86 ± 0.18	-0.31 ± 0.15	27.71 ± 0.12	1.76	$1.73^{+0.06}_{-0.05}$	$7.7^{+0.9}_{-1.3}$	
HFF4C										
4025-5027 ^f	i1 ^f	177.417749	+22.417435	0.57 ± 0.03	0.02 ± 0.02	25.19 ± 0.02	1.58	$1.60^{+0.12}_{-0.12}$	$7.5^{+0.8}_{-0.8}$...
4024-4492	Y2	177.417702	+22.413687	1.61 ± 0.42	0.35 ± 0.18	27.26 ± 0.11	1.63	$1.68^{+0.22}_{-0.14}$	$8.4^{+1.0}_{-0.9}$...

^a For simplicity, the part that represents the cluster name is omitted. Examples of full IDs are HFF1C-2508-2496 and HFF1C-Y1.

^b Short ID used only in this paper for simplification and clarity.

^c Total magnitude.

^d Median value and 1σ error of the magnification factor from the MCMC posterior distribution.

^e L₁₄ = Laporte et al. (2014), A₁₄ = Atek et al. (2014), WZ₁₄ = Zheng et al. (2014), I = Ishigaki et al. (2015), L₁₅ = Laporte et al. (2015), A₁₅ = Atek et al. (2015a), C = Coe et al. (2015), M = McLeod et al. (2015).

^f Selected by our two criteria for *i*-dropout and *Y*-dropout galaxies.

Table B3
Dropout galaxy candidates at $z \sim 9$ in the four HFF cluster fields.

ID ^a	ID ^{a,b}	R.A.	Decl.	$YJ^c - JH_{140}$	$JH_{140} - H_{160}$	H_{160} ^d	μ_{best}	μ^e	z_{photo}	Reference ^f
HFF1C										
2481-2561 ^g	Y2 ^g	3.603379	-30.382255	0.78 ± 0.09	-0.05 ± 0.07	26.69 ± 0.05	1.40	$1.49^{+0.08}_{-0.06}$	$8.2^{+0.9}_{-0.9}$	WZ ₁₄ , I, A ₁₅
2492-2561 ^g	Y5 ^g	3.603859	-30.382262	1.12 ± 0.18	0.19 ± 0.09	26.79 ± 0.06	1.40	$1.48^{+0.08}_{-0.06}$	$8.4^{+0.9}_{-0.9}$	WZ ₁₄ , I, A ₁₅ , M
2220-4053	YJ3	3.592512	-30.401486	> 1.21	0.55 ± 0.27	27.38 ± 0.15	14.12	$14.37^{+1.22}_{-0.90}$	$9.6^{+1.0}_{-7.1}$	AZ, I, O
HFF2C										
1151-4540 ^g	Y1 ^g	64.047984	-24.081671	0.97 ± 0.10	0.00 ± 0.06	26.50 ± 0.04	1.43	$1.44^{+0.04}_{-0.04}$	$8.4^{+0.9}_{-0.9}$	L ₁₅ , C, M
0939-5354 ^g	Y2 ^g	64.039161	-24.093184	1.27 ± 0.16	0.06 ± 0.07	26.55 ± 0.05	1.39	$1.39^{+0.03}_{-0.03}$	$8.5^{+0.9}_{-0.9}$	L ₁₅ , M
0901-5172 ^g	Y3 ^g	64.037566	-24.088113	1.06 ± 0.27	-0.25 ± 0.19	27.82 ± 0.14	1.70	$1.71^{+0.06}_{-0.06}$	$8.3^{+1.0}_{-0.9}$	L ₁₅ , C, M
HFF4C										
3358-4457	YJ1	177.389950	+22.412711	> 2.39	0.19 ± 0.05	25.80 ± 0.03	17.51	$6.44^{+21.86}_{-3.64}$	$9.2^{+1.0}_{-1.0}$	WZ ₁₂
4024-4492 ^g	Y2 ^g	177.417700	+22.413691	1.11 ± 0.23	-0.15 ± 0.16	27.44 ± 0.11	1.63	$1.69^{+0.23}_{-0.14}$	$8.4^{+0.9}_{-0.9}$...
3373-4483	YJ3	177.390553	+22.413417	> 1.30	0.15 ± 0.26	27.75 ± 0.16	63.34	$18.30^{+40.36}_{-12.02}$	$8.7^{+0.9}_{-6.7}$...
3617-3327	YJ4	177.400727	+22.392425	> 1.28	-0.17 ± 0.28	27.89 ± 0.20	35.85	$41.22^{+12.10}_{-7.02}$	$8.5^{+0.9}_{-1.0}$...

^a For simplicity, the part that represents the cluster name is omitted. Examples of full IDs are HFF1C-2481-2561 and HFF1C-Y2.

^b Short ID used only in this paper for simplification and clarity.

^c $YJ \equiv (Y_{105} + J_{125})/2$

^d Total magnitude.

^e Median value and 1σ error of the magnification factor from the MCMC posterior distribution.

^f WZ₁₂ = Zheng et al. (2012), AZ = Zitrin et al. (2014), WZ₁₄ = Zheng et al. (2014), I = Ishigaki et al. (2015), L₁₅ = Laporte et al. (2015), A₁₅ = Atek et al. (2015a), C = Coe et al. (2015), M = McLeod et al. (2015), O = Oesch et al. (2015).

^g Selected by our two criteria for *Y*-dropout and *YJ*-dropout galaxies.